Multimodal Imaging of Pancreatic Cancer Microenvironment in Response to an Antiglycolytic Drug

Elnaz Sheikh, Kirti Agrawal, Sanjit Roy, David Burk, Fabrizio Donnarumma, Young H. Ko, Praveen Kumar Guttula, Nrusingh C. Biswal, Hem D. Shukla*, Manas Ranjan Gartia**

E. Sheikh, K. Agrawal, M. R. Gartia
Department of Mechanical and Industrial Engineering, Louisiana State University, Baton Rouge, LA 70803, USA
mgartia@lsu.edu

S. Roy, N. C. Biswal, H. D. Shukla
Department of Radiation Oncology, University of Maryland School of Medicine, Baltimore, MD 21201, USA
Nrusingh.Biswal@umm.edu
hdshukla@som.umaryland.edu

D. Burk
Pennington Biomedical Research Center, Baton Rouge, LA 70808, USA

F. Donnarumma
Department of Chemistry, Louisiana State University, Baton Rouge, Louisiana 70803, USA

Y. H. Ko
NewG Lab Pharma, 701 East Pratt Street, Columbus Center, Baltimore, MD 21202, USA

Praveen Kumar Guttula
Sprott Center for Stem Cell Research, Regenerative Medicine Program, Ottawa Hospital Research Institute, Ottawa, ON, Canada
Department of Biochemistry, Microbiology, and Immunology, Faculty of Medicine, University of Ottawa, Ottawa, ON, Canada

Keywords: Raman spectroscopy, 3-bromopyruvate, cancer microenvironment, glycolysis, Warburg effect, lipid metabolism, pancreatic cancer

Abstract

Lipid metabolism and glycolysis play crucial roles in the progression and metastasis of cancer, and the use of 3-bromopyruvate (3-BP) as an antiglycolytic agent has shown promise in killing pancreatic cancer cells. However, developing an effective strategy to avoid chemoresistance requires the ability to probe the interaction of cancer drugs with complex tumor-associated microenvironments (TAMs). Unfortunately, no robust and multiplexed molecular imaging technology is currently available to analyze TAMs. In this study, we demonstrate the simultaneous profiling of three protein biomarkers using SERS nanotags and antibody-functionalized nanoparticles in a syngeneic mouse model of pancreatic cancer. This allows for comprehensive information about biomarkers and TAM alterations before and after treatment. Our multimodal imaging techniques include surface-enhanced Raman spectroscopy (SERS), immunohistochemistry, polarized light microscopy, second harmonic generation (SHG) microscopy, fluorescence lifetime imaging microscopy (FLIM), and untargeted liquid chromatography and mass spectrometry (LC-MS) analysis. The study reveals the efficacy of 3-BP in treating pancreatic cancer and identifies drug treatment-induced lipid species remodeling and associated pathways through bioinformatics analysis.

1. Introduction

Pancreatic cancer (PC) is the fourth leading cause of cancer-related death in the US. Most PC patients (> 50%) are diagnosed at an advanced stage where the 5-year survival rate is 3%.[1] The surgical removal of pancreatic tumor cells (Whipple procedure) can increase the survivability of the patients. However, less than 20% of patients are eligible for surgery due to regional and distant metastasis during these end stages. Further, chemotherapy and radiation therapy are ineffective for advanced-stage patients. Hence, there is an unmet need to develop new treatment options for PC.

3-bromopyruvate (3-BP) is an alkylating agent and has been shown to have potent antitumor activities in several types of cancers,[2] including PC.[3] Collagen-rich, weakly vascularized, and extremely hypoxic non-neoplastic stroma are among pancreatic tumor tissue's distinguishing cellular and non-cellular features.[4] Often, these traits are linked to chemoresistance to the most widely used anticancer drugs. Thus, there is a need to understand the interaction of 3-BP with the tumor microenvironment.

The tumor microenvironment is complex, and typical components include collagen, proteins, DNA, lipids, and varied cell types (macrophage, epithelial cells, stroma, normal cells, and cancer cells). A single tool might not be sufficiently sensitive to probe all the components of the tumor microenvironment. Lipids exhibit a significantly greater Raman scattering cross section in comparison to collagen.[5] Despite being present in significant amounts within the extracellular matrix, glycosaminoglycans show weak Raman cross-sections.[6] Similarly, the Raman cross-section of DNAs is typically larger than that of proteins [7]. On the other hand, the second harmonic generation (SHG) cross-section for collagen (Collagen I and III) is high and can be easily imaged in a tissue.[8] Therefore, a multimodal approach could be useful in interrogating a complex tumor microenvironment.

Pancreatic tumor cells alter their cellular glucose metabolism to fulfill their elevated energy demands. This is accomplished through heightened glycolysis, resulting in increased consumption of glucose and the production of ATP and lactic acid, which fuel the tumor's growth and aggressive behavior.[9] Tumor cells enhance the expression of lactate transporters to facilitate their high glucose consumption and lactic acid production, which enables them to import surplus glucose and export excessive lactic acid. Interestingly, 3-BP is transported into the cells through lactate transporters. Hence, 3-BP can be selectively transported into the cancer cells compared to normal cells. Hexokinase 2 (HK2) is a vital enzyme in glucose metabolism through aerobic glycolysis.[9b, 10] 3-BP irreversibly alkylates HK2, disrupting glucose metabolism and leading to cancer cell death.[11] In addition, 3-BP kills cells by producing reactive oxygen species (ROS).[12] However, the effect of 3-BP on lipid remodeling, the spatial distribution of proteins, and metabolic activity have not been well investigated. Here, we have created a

syngeneic in vivo model using a highly aggressive pancreatic cancer cell (Panc-2) to study the effect of 3-BP.

Previously, we have shown the efficacy of 3-BP in killing PC cells in vitro and in vivo.[3b] Our previous study showed that 3-BP inhibits glycolysis, ATP, lactic acid production, and expression of HK2. Furthermore, in vivo study showed that a 20 mg/kg dose level of 3-BP reduced tumor growth by ~ 80%. Here, we showed the spatial mapping of three different proteins (transforming growth factor- β1 (TGFβ1), HK2, Caspase3) simultaneously on the tumor tissues using surface-enhanced Raman spectroscopy (SERS)-encoded Raman nanoparticle imaging.

Multiplexed biomarker profiling is crucial for the diagnosis of cancer and for assessing the effectiveness of therapies. As a semiquantitative method, immunohistochemistry (IHC) is currently the accepted method of detecting biomarkers in clinical samples. Histochemistry is the conventional method to visually examine the gross tissue morphology, cell type, subcellular structure through the reaction of certain dyes and stains with endogenous chemicals that are present to form colored compounds.[13] IHC, however, can only probe one or a small number of biomarkers at once in a sample.[14] Furthermore, the utilization of many chemical constituents is restricted in traditional histochemistry, thereby constraining its applicability. There are several alternative methods for finding multiple targets in a sample, including mass spectrometry,[15] protein chips,[16] RT-PCR,[17] spatial transcriptomics,[18] and fluorescence assay.[19] However, most of these methods are destructive and necessitate laborious sample preparation. In addition, the sample preparation could destroy the three-dimensional architecture of cells and tissues. Further, the broad emission peaks (> 30 nm) in fluorescence imaging typically lead to spectral cross-talk in multiplexed imaging. Raman spectroscopy and microscopy provide sensitive, quantitative, and noninvasive techniques that can detect molecular-level variations through specific fingerprints, offering significant advantages over alternative methods.[20] Because of SERS nanotag's high sensitivity [21] and small spectral peak width of 1-2 nm,[22] multiplexed detection is feasible. However, typical SERS nanotags often use thiol-conjugated molecules, which are unstable and prone to oxidation.[23] Furthermore, conventional Raman reporters have several peaks in the fingerprint region (1000-1700 cm^{-1}) that frequently overlap and could lead

to cross-talk.[24] Additionally, the SERS signal may overlap with various tissue or cell background signals produced from naturally occurring biological molecules, including proteins, phospholipids, cytochromes, etc. Consequently, using SERS nanotags with excellent spectral resolution and low background interference is necessary. Although several researchers have classified the cell and tissue samples with overlapped Raman peaks in the fingerprint regions using the Raman unmixing method, only a broad class of cell/tissue features could be obtained (e.g. lipids, proteins, collagen, DNA, glycogen etc.).[25] Nonetheless, there hasn't been a strong demonstration of using spontaneous Raman spectroscopy to perform spatial imaging of multiple proteins or lipid subspecies (e.g. PC 42:4 versus PC 42:6).[26]

Previous researchers have made SERS nanotags using Raman reporters moieties such as alkynes ($-C \equiv C -$, Raman peak at ~ 2230 cm^{-1}), nitriles ($-C \equiv N$, Raman peak at ~ 2120 cm^{-1}), azides ($-N_3$, Raman peak at ~ 2073 cm^{-1}), and deuterium ($C - D$, Raman peak at ~ 2150 cm^{-1}) that display distinctive vibrational peaks in the Raman silent region (1800 – 2800 cm^{-1}).[27] Raman silent region is free from interference due to the Raman signal of endogenous biological substances making these probes highly suitable for multiplexed detection.

Here, we developed SERS nanotags using AuNP core and anchored alkyne (using trimethyl(phenylethynyl)silane (TPS); designated as tag1), deuterium (using Dimethyl sulfoxide-d6 (D-6); tag2), and nitrile (using 4-Mercaptobenzonitril (4-MB; tag3) moieties via $\sigma - \pi$,[28] and $\pi - \pi$ [29] interactions. These Raman reporters (RRs) exhibit peaks in Raman-silent spectral region without any overlap with each other. We used polydopamine (PDA) as a protective biocompatible layer thanks to its preferable characteristics, such as self-polymerization and adhering capability to the surface of NPs. PDA allows the incorporation of any Raman reporters (even without amine or thiol group) on to the AuNP surface.[30] The RR is conjugated to the PDA layer through the dopamine quinone group utilizing Michael addition.[31] These characteristics, biodegradability, and chemical reactivity with other molecules make them a unique choice for fabricating SERS tags, resulting in a novel SERS imaging platform. Moreover, catechol, amine, and imine as functional groups on the surface of these tags enhance their reactivity with other groups in other biomolecules and antibodies.[32] Our main motivation for developing SERS nanotags is to simultaneously profile lipids, collagen and specific proteins of interest (TGFβ1,

HK-2, Caspase 3) in the tumor microenvironment (TME). The Raman fingerprint regions (100 – 1800 cm^{-1}) were utilized to profile the lipids and collagens. The Raman silent regions (1800 – 2800 cm^{-1}) were utilized to profile the proteins. Simultaneous profiling of lipids, collagen and proteins are not possible with a single IHC marker. The antibody conjugated nanotags allowed us to profile and image three different proteins simultaneously with high specificity without any Raman peak overlaps. The intensity distribution of Raman peaks at 2018 cm^{-1}, 2112 cm^{-1}, and 2224 cm^{-1} allowed us to profile TGFβ1, Caspase3, and HK2 respectively.

We used a one-pot synthesis approach; NPs, RRs, and PDA as protective layers were compacted to provide the SERS immunoassays with distinctive flavors. Each flavor of probes was then conjugated with an antibody— TGFβ1 (designated as tag1), Caspase-3 (defined as tag2), and Hexokinase 2 (designated as tag3) tumor-associated proteins expressed in pancreatic cancer microenvironment (TAM) in the syngeneic pancreatic cancer tissue to create a multicolor image of three biological targets. We used these antibody-conjugated-SERS nanotags to identify separate and multiple cancer biomarker changes in response to the drug treatment. To validate the efficacy of the 3-bromopyruvate (3-BP) drug, we further analyzed the untreated and treated tumor tissues. We used polarized light microscopy, immunohistochemistry, two-photon and second harmonic generation (SHG) microscopy, fluorescence lifetime imaging microscopy (FLIM), and liquid chromatography-mass spectrometric (LC-MS) measurements method to probe the tissue samples.

2. Results and Discussions

2.1. Design and characterization of SERS immunoassays

Figure 1A schematically shows the approach used in the present work. The saline-treated (MOCK group) and 3-BP treated (3-BP group) tumor tissues were processed and incubated with the antibody-conjugated SERS nanotags. Using Raman microscopy, the SERS nanotags comprised three different RRs and antibodies for detecting three corresponding proteins on the tissue. Three different types of SERS nanotags were prepared by applying a one-pot synthesis approach. First, the surface of gold nanoparticles (Au NPs) was immobilized with three different

RRs—4-MB, D-6, and TPS—and then, using a self-polymerization process, a layer of PDA was coated on top of them for capturing antibodies. Their respective antibodies were conjugated on the surface of SERS nanotags to identify HK2, Caspase3, and TGFβ1 antigens in tissues. The Raman signatures of the proteins are shown in **Figure 1B**. The corresponding Raman peak assignments are provided in **Tables S1-S3**. All SERS nanotags were confirmed by Raman spectroscopy (**Figure 1C**). The related Raman peak assignments for the Raman reporters are provided in **Tables S4-S6**. Figure 1C showed characteristics signals at 2018, 2116, and 2225 cm^{-1} in the Raman silent region for each type of SERS nanotags. The characteristics peak at 2018, 2116, and 2225 cm^{-1} are due to the RR with TPS (red curve), D-6 (blue curve), and 4-MB (green curve), respectively (**Figure 1C**). The figure also illustrates the successful immobilization of the respective RRs on the surface of Au NPs. UV-vis spectra in **Figure 1D** depict plasmon resonance shifts due to surface modification with RRs and Dopamine. The surface plasmon peak was observed at 533 ± 3 nm due to the Au NPs.[33] The intensity of the surface plasmon peak intensified and red-shifted in peak wavelength after PDA coating **(Figure 1D)**. Dynamic light scattering (DLS) measurements (**Figure 1E**) reveal that the average hydrodynamic size of the Au NPs increased from 60 ± 5 nm to 90 ± 15 nm after PDA coating. After 4-MB addition, the hydrodynamic diameter changed to 100 ± 20 nm. A transmission electron microscopy (TEM) image (**Figure 1F, 1G, 1H**) of SERS nanotags— Au-Dopamine+4-MB, Au-Dopamine+TPS, and Au+Dopamine+D6—shows the approximate size of the NPs as 60 ± 5 nm.

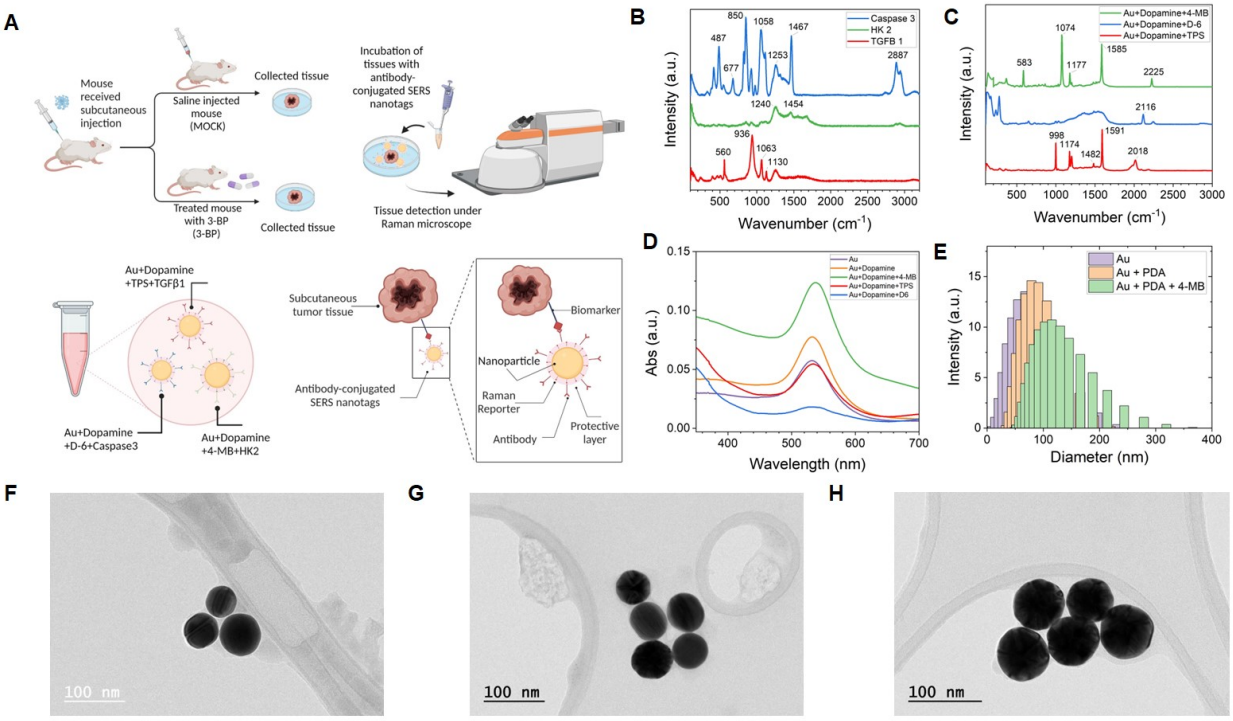

Figure 1. Schematic overview of multiplexed SERS imaging of biomarkers in a subcutaneous tumor model of pancreatic cancer and characterization of Raman reporters. **(A)** Workflow showing the preparation of antibody-conjugated SERS nanotags to perform Raman microscopy of tumor tissues. **(B)** Raman spectra of TGFβ1, HK2, and Caspase3 antibodies show each protein's characteristic Raman peaks. **(C)** SERS spectra of three nanotags (4-MB, D-6, and TPS) without antibodies. **(D)** UV-Vis spectra of all three SERS nanotags show the plasmonic peak near 530 nm. **(F)** Dynamic light scattering (DLS) results show the distribution of hydrodynamic diameters of nanoparticles (Au) and nanoparticles conjugated with one of the SERS nanotags (Au+Dopamine, Au+Dopamine+4-MB). **(F)** Representative TEM image of one SERS nanotag (Au+Dopamine+4-MB). **(G)** Representative TEM image of one SERS nanotag (Au+Dopamine+TPS). **(H)** Representative TEM image of one SERS nanotag (Au+Dopamine+ D-6).

2.2. Morphological and IHC imaging of Pancreatic cancer tissues

Figure 2A shows morphological changes in the tumor following 3-BP treatment (3-BP) compared to saline treatment (MOCK). The tumor volume decreased by 60-80% following 3-BP treatment (**Figure 2B**). **Figure 2C** depicts the mRNA expression level changes, in which HK2 expression level decreased significantly in the 3-BP group in response to two different concentration levels of 3-BP, 20 and 40 μM, compared to the MOCK group. The Western blot

analysis in Panc-2 cancer cells also showed down regulation of HK2 after 3-BP treatment [3b]. Based on the pixel intensity of the H&E images (see Supporting Information **Figure S1A and S1B**), a significantly higher ($P < 0.001$) cytoplasm content was seen in the 3-BP group compared to the MOCK group. The data showed necrotic tissues in 3-BP-treated tissue samples compared to the MOCK group. We also have performed several experiments to show the features of TME. Both the MOCK and 3-BP tissues showed the blood vessels after H& E (Hematoxylin and Eosin) staining (see Supporting Information **Figure S1C**). The existence of tumor fibroblast in tissue samples have been confirmed by staining of same sample tissue, used in this study with antibody, α-SMA and vimentin (see Supporting Information **Figure S1D**) which are known marker for cancer associated fibroblast as described by others. [34] Both markers which are expressed in cancer associated fibroblast (CAFs cells) are component of TME (tumor microenvironment). The α-SMA is involved in cell contractility, structure and integrity of cell and promote tumor cell proliferation, immune suppression and impede drug delivery. Vimentin (EMT marker) also regulate cell motility structure and integrity, involve in cell invasion and metastasis in pancreatic cancer. [35]

Figure 2D shows the results of immunohistochemistry (IHC) imaging. The microenvironment of pancreatic cancer contains several factors, such as tumor-associated macrophages (TMs), inflammatory cytokines, and macrophages, that contribute to the resistance of drug and radiation therapies. Further, these factors can be upregulated and exacerbate tumor progression.[36] Moreover, TMs can enhance tumor growth, progression, and invasiveness by releasing growth factors and mediators by suppressing immune cells' anticancer responses.[37] We utilized Ionized calcium-binding adapter molecule 1 (Iba1) to examine TMs. Iba1 has been used frequently as a marker for microglial cells. More recently, it was also recognized as a "pan-macrophage marker" because it is expressed by all monocyte cell subpopulations/macrophage lineage.[38] We used Iba1 to detect the level of macrophages in both MOCK and 3-BP tissues **(Figure 2D)**. The brown color indicates the expression level of Iba1. The calculated pixel intensity values of images (**Figure 2E**) revealed that the Iba1 expression level of the 3-BP treated group is significantly lower ($P < 0.001$) compared to the MOCK group demonstrating the effectiveness of 3-BP treatment. We also compared the expression level of TGFβ1, HK2, and

Caspase3 before (MOCK) and after 3-BP treatment **(Figures 2F, 2H, and 2J)**. The pixel intensity values of images demonstrated a significant decrease in the expression level of TGFβ1 **(Figure 2G)** and HK2 **(Figure 2I)** and a significant increase in the expression level of Caspase3 **(Figure 2K)** in the 3-BP groups in comparison with MOCK groups.

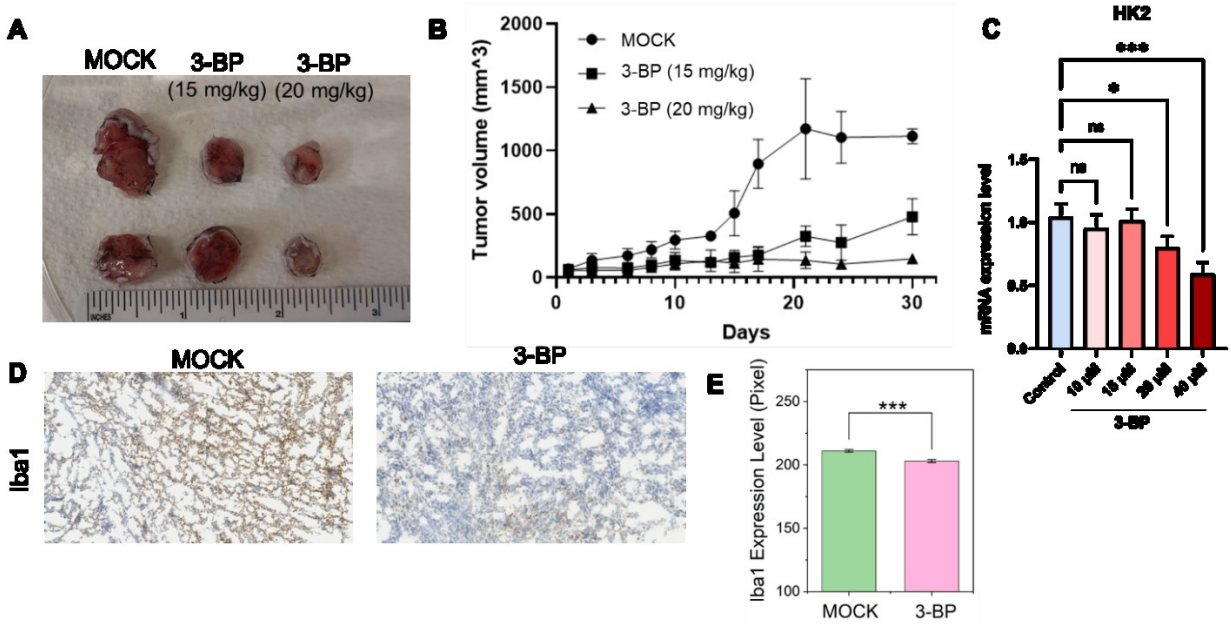

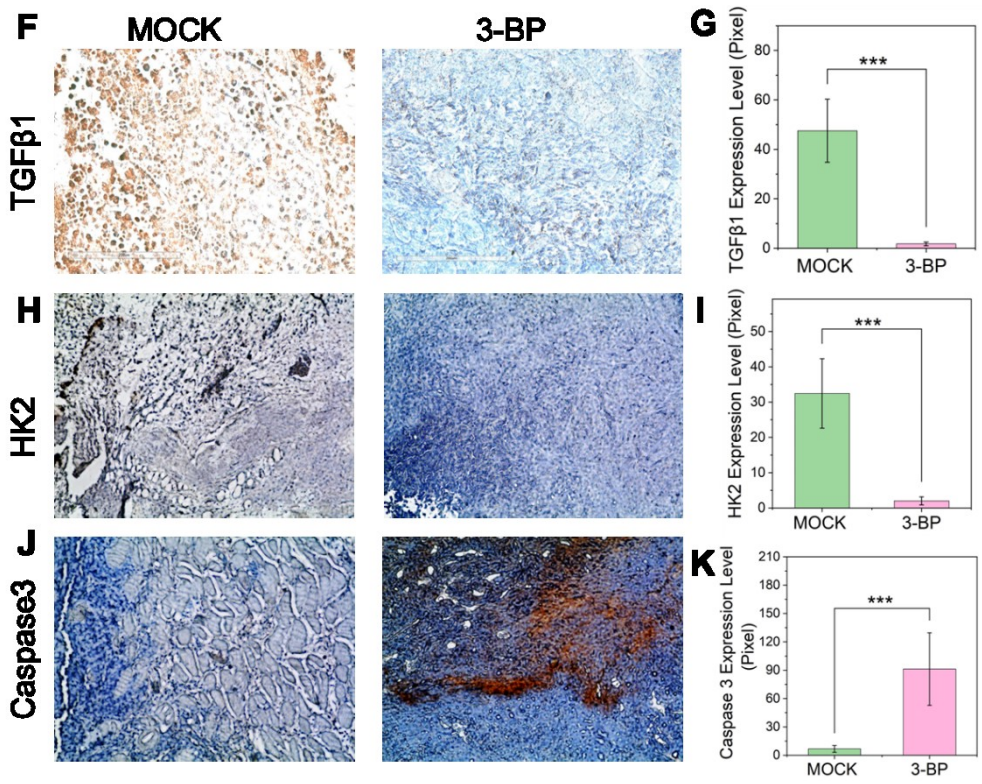

Figure 2. Structural and immunohistochemical (IHC) imaging of subcutaneous tissue from tumor model of pancreatic cancer before and after 3-BP treatment. **(A)** Representative images of the tumor before (MOCK) and after (3-BP) treatment. The image shows the response to two different concentrations of 3-BP treatments (15 and 20 mg/kg). **(B)** Comparison of tumor volume on different days before and after treatment (n = 4/group). **(C)** Comparison of the mRNA expression level of HK2 in control versus 3-BP groups treated with different concentrations of 3-BP (10 μM, 15 μM, 20 μM, 40 μM). **(D)** IHC image showing the expression level of Iba1 in MOCK and 3-BP tissue. **(E)** Comparison of Iba1 expression level (brown color) of MOCK and 3-BP tissue. Representative IHC images in MOCK and 3-BP groups showing the expression level of **(F)** TGFβ1, **(H)** HK2, and **(J)** Caspase 3. Comparison of **(G)** TGFβ1, **(I)** HK2, **(K)** Caspase 3 expression levels (brown color) of MOCK and 3-BP tissue. The plot shows the differences in pixel intensity of the MOCK and 3-BP groups in Figs. 2E, G, I, and K (n = 3/group). The error bars show the standard deviation. *P<0.05, **P<0.01, ***P<0.001

2.3. Raman imaging of cancer tissues

To profile TGFβ1, HK2, and Caspase3 proteins and evaluate their expressions in both groups, we first probed each tissue type with one antibody-conjugated SERS nanotags. **Figure**

3A shows the bright field images of tissues studied for each type of nanotag. Next, we obtained the Raman map of the indicated area and analyzed each image using the empty modeling method to generate mapping data (**Figure 3B**). The details about empty modeling are provided in the Supporting Information (**Figures S2-S5**). This method is proper when no spectra are available for the components. Each Raman image comprises ~ 40.5 x 10^6 data points (45,000 spectra, and 900 points per spectra). The analyzed images using this method can identify significant biochemical features of the sample and the associated mean Raman spectra. **Figure 3B** shows the Raman mapping images collected from stained tissues with each type of nanotag (red color, tag1: Au + Dopamine + TPS + TGFβ1; blue color, tag2: Au + Dopamine + D-6 + Caspase3; green color, tag3: Au + Dopamine + 4-MB + HK2). Each color in the heat map is associated with the expression of the related biomarkers, which is as follows: red = TGFβ1; green = HK2; and blue = Caspase3. The merged Raman map for the tissue background and the respective nanotags are shown in **Figure 3C**. The MOCK group showed a higher expression of TGFβ1 (red color) as well as HK2 (green color) and lower expression of Caspase3 (blue color), respectively, compared to the 3-BP group **(Figure 3B)**. **Figures 3D, 3E, and 3F** show different magnifications of SEM images captured from stained MOCK tissue with tag1, representing the presence of nanotags on the surface of the tissue. The EDS layered images (**Figures 3G-3I**) of the tissue revealed Au footprint on the surface of the tissue, confirming the presence of nanotags with the Au nanoparticles as the core **(Figure 3I)**. **Figures 3J, 3K, and 3L** display SEM images at various magnifications that were taken from stained 3-BP tissue with tag1, indicating the presence of nanotags on the tissue's surface. The Au footprint on the tissue's surface was detected in the EDS layered images (**Figures 3M–3N**), which supported the existence of nanotags with Au nanoparticles as the core (**Figure 3O).** The SEM and EDS images of the 3-BP and MOCK tissues with all tags can be seen in the Supporting Information (**Figures S6A-S6L**).

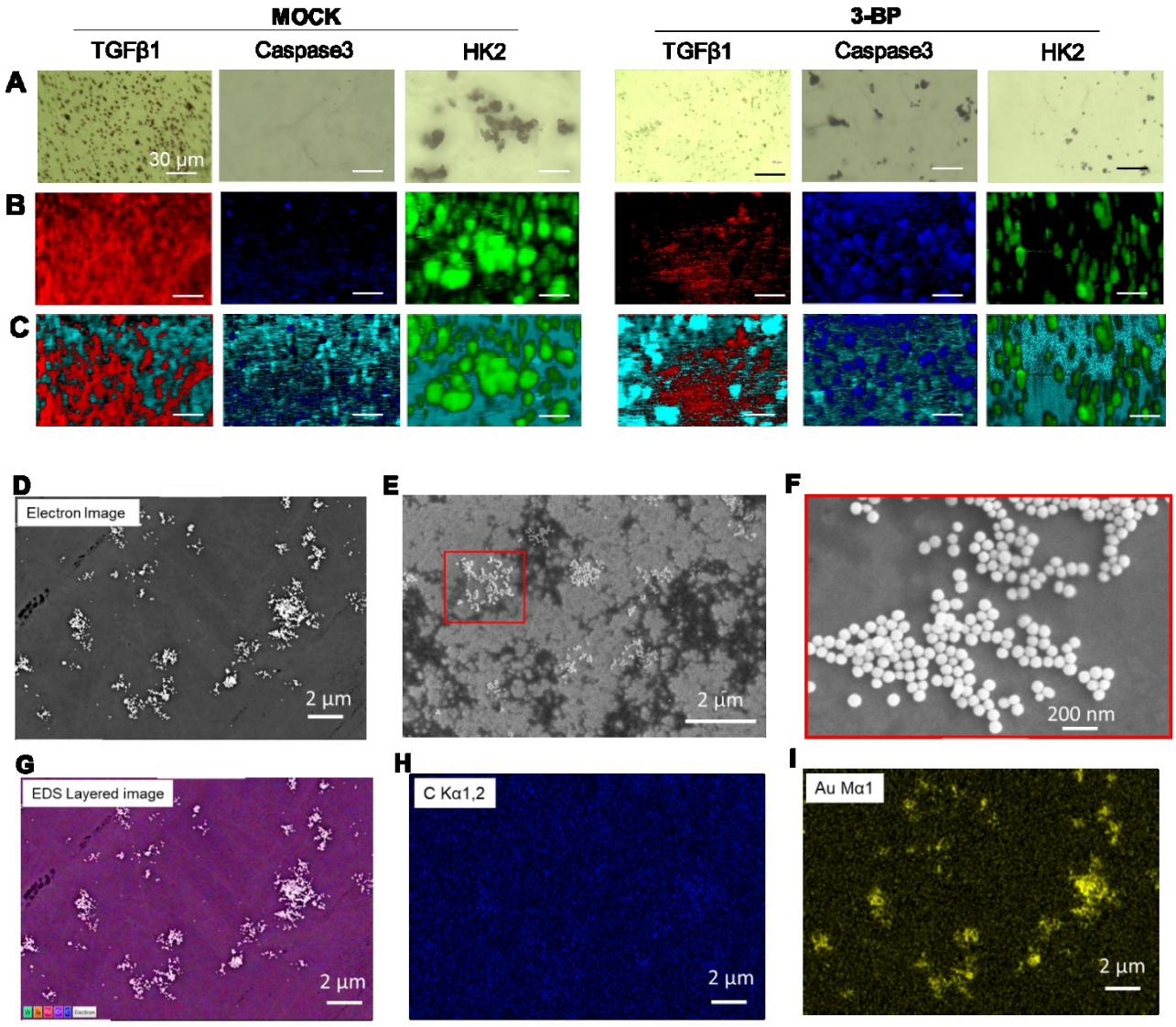
MOCK
3-BP
TGFβ1
Caspase3
HK2
TGFβ1
Caspase3
HK2
A
B
C
30 μm
D
Electron Image
2 μm
E
2 μm
F
200 nm
G
EDS Layered image
2 μm
H
C Kα1,2
2 μm
I
Au Mα1
2 μm

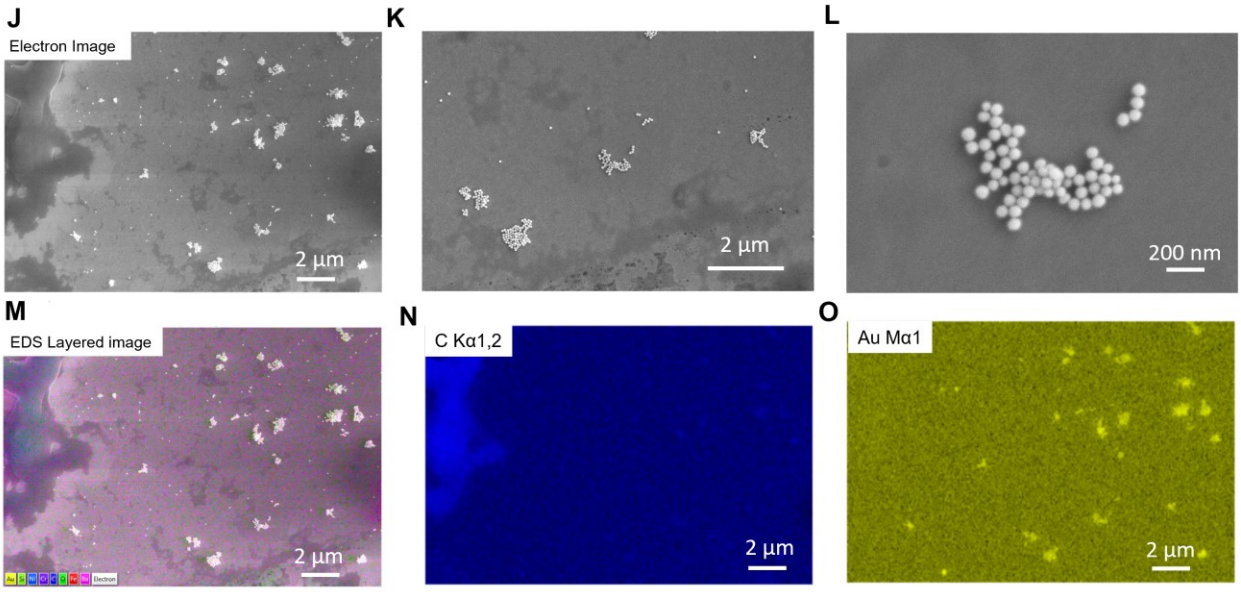

Figure 3. SERS-based molecular imaging of the subcutaneous tumor model of pancreatic cancer. **(A-C)** Representative SERS mapping image of tumor tissue before (MOCK group) and after (3-BP group) 3-BP treatment. The figures show **(A)** brightfield, **(B)** SERS mapping, and **(C)** merged images. SERS mapping was carried out using nanoparticles coated with anti-TGFβ1 and TPS (tag1) (n = 49,383 spectra), anti-Caspase3 and D-6 (tag2) (n = 48,125 spectra), and anti-HK2 and 4-MB (tag3) (n = 50,861 spectra) as protein targets and Raman encoding molecules, respectively. The spatial resolution of these images is 0.5 µm. The same SERS tags were used for both MOCK and 3-BP tissues. The scale bar represents 30 µm. **(D)** Scanning electron microscopic (SEM) images of the MOCK tissue probed with tag1 (TGFβ1 and TPS). **(E, F)** zoomed in image of the AuNPs, **(G)** the corresponding Energy-dispersive X-ray spectroscopy (EDS) image of the tissue **(H)** EDS map of C Kα1,2, and **(I)** EDS map of Au Mα1 surface profile on the tissue. **(J)** Scanning electron microscopic (SEM) images of the 3-BP tissue probed with tag1 (TGFβ1 and TPS). **(K,L)** zoomed in image of the AuNPs, **(M)** the corresponding Energy-dispersive X-ray spectroscopy (EDS) image of the tissue **(N)** EDS map of C Kα1,2, and **(O)** EDS map of Au Mα1 surface profile on the tissue.

Raman spectra of the MOCK and 3-BP groups were obtained to show the biochemical changes to the specific biomarkers in the tumor tissues before and after the treatment (**Figure 4A – 4C**). The associated Raman peak for TGFβ1 (2017 cm^{-1}) showed higher intensity for the MOCK group than the 3-BP group **(Figure 4A)**. The comparison of the intensity of the corresponding Raman peak at 2111 cm^{-1} for tag2 illustrates a higher expression of Caspase3 protein in 3-BP treated tissue than in the saline-treated (MOCK) tissue (**Figure 4B**). The tissues stained with tag3, which targets HK2 with the corresponding Raman peak at 2228 cm^{-1}, showed

high expression of HK2 in MOCK tissues compared to the 3-BP treated tissues (**Figure 4C**). We also quantitatively compare the Raman maps **(Figure 3B)** for each tissue with corresponding tags; we calculated their pixel intensities using ImageJ. We found a significant decrease ($P < 0.001$) in the expression level of TGFβ1 (**Figure 4D**) and HK2 (**Figure 4F**) after the 3-BP treatment and a significant increase ($P < 0.001$) in the expression level of Caspase3 (**Figure 4E**) in the 3-BP treated tumor tissues. In addition, principal component analysis (PCA) plots made by Raman speectra collected from the tissues stained with each nanotag, (TGFβ1, HK2, Caspase3, and all tags), show cluster between MOCK and 3-BP groups (**Figure 4G-4J).**

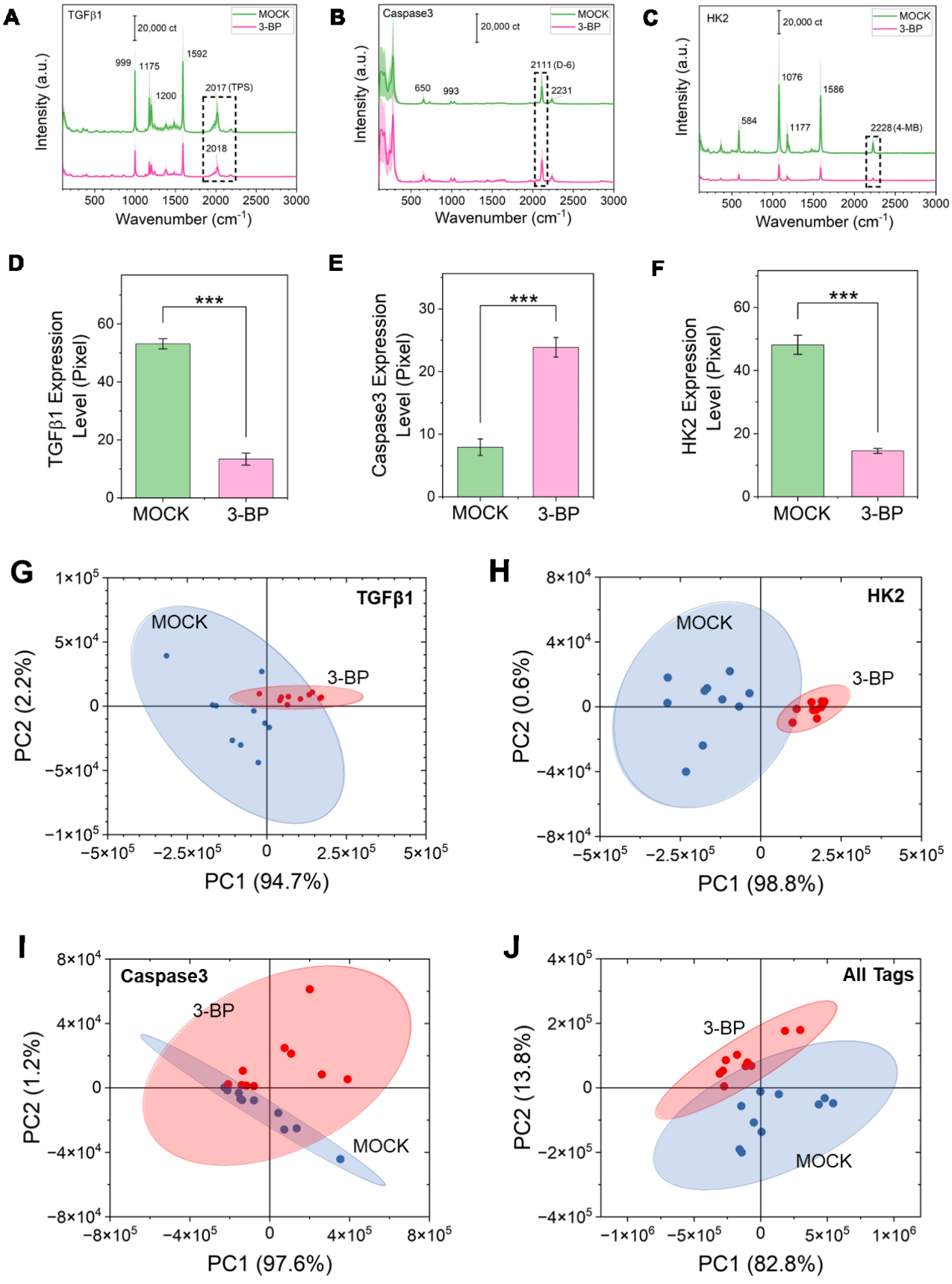
A
TGFβ1
20,000 ct
MOCK
3-BP
999
1175
1200
1592
2017 (TPS)
2018
Intensity (a.u.)
Wavenumber (cm-1)
B
Caspase3
20,000 ct
MOCK
3-BP
650
993
2111 (D-6)
2231
Intensity (a.u.)
Wavenumber (cm-1)
C
HK2
20,000 ct
MOCK
3-BP
584
1076
1177
1586
2228 (4-MB)
Intensity (a.u.)
Wavenumber (cm-1)
D
TGFβ1 Expression Level (Pixel)
***
MOCK
3-BP
E
Caspase3 Expression Level (Pixel)
***
MOCK
3-BP
F
HK2 Expression Level (Pixel)
***
MOCK
3-BP
G
TGFβ1
MOCK
3-BP
PC2 (2.2%)
PC1 (94.7%)
H
HK2
MOCK
3-BP
PC2 (0.6%)
PC1 (98.8%)
I
Caspase3
3-BP
MOCK
PC2 (1.2%)
PC1 (97.6%)
J
All Tags
3-BP
MOCK
PC2 (13.8%)
PC1 (82.8%)

Figure 4. Comparison of SERS spectra of MOCK and 3-BP groups for **(A)** TGFβ1 and TPS (n = 45,257 spectra), **(B)** Caspase3 and D-6 (n = 48,675 spectra), and **(C)** HK2 and 4-MB (n = 48,321 spectra). The standard deviation of spectra showed a shaded color around average spectra. The intensity comparison in the Raman silent regions (shown by dotted box) clearly showed the decrease in the expression level of TGFβ1 and HK2 after 3-BP treatment **(A & C)**. The result also showed an increase in the expression level of Caspase3 after 3-BP treatment **(B)**. The vertical bar corresponds to an intensity of 20,000 counts in each figure. The comparison of the expression level of proteins calculated from the corresponding SERS mapping images are shown for **(D)** TGFβ1, **(E)** Caspase3, and **(F)** HK2. PCA score plots for the first and second principal components of MOCK and 3-BP groups are shown for **(G)** TGFβ1, **(H)** Caspase3, **(I)** HK2, and **(J)** all three nanotags. Statistical significance was measured using a two-tailed Student's paired t-test with n = 30 for each group. *P<0.05, **P<0.01, ***P<0.001.

We further performed multiplexed imaging of the tissues by mixing all three antibody-conjugated SERS nanotags. **Figure 5A** shows bright field images of tissues probed with a mixture of all three antibody-conjugated SERS nanotags. The corresponding Raman maps are shown in (**Figures 5B – 5F**). We analyzed the Raman maps using the empty modeling method to find significant biochemical components and the related spectrum. MOCK and 3-BP groups showed three components: tag1, tag2, and tag3 (**Figures 5B – 5D**). The fourth component was found to be the tissue background (**Figure 5E**). The merged images of all the tags are shown in (**Figure 5F**). The MOCK tissue group stained with the mixture of all tags showed higher expression of TGFβ1 and HK2 and lowered expression of Caspase3 compared to the 3-BP tissue group. **Figure 5G** illustrates the Raman spectra of tissues probed with the mixture of antibody-conjugated SERS nanotags showing simultaneous detection of their peaks with no interference (**also see Table S7**). **Figure 5H** represents extracted Raman spectra of each component shown in **Figures 5B – 5D**. These results showed successful simultaneous detection of multiple biomarkers using SERS nanotags. Moreover, based on the Raman results of these tissues with the respective biomarkers, downregulation of TGFβ1 and HK2 and upregulation of Caspase3 were observed after the 3-BP treatment.

The findings suggest that the administration of 3-BP to mice led to a decrease in fibrosis and cell proliferation. This may be attributed to the crucial role of TGFβ1 in promoting cell transformation and the process of epithelial-to-mesenchymal transition while also inhibiting

apoptosis. The diminished expression of HK2 indicated a significant reduction in ATP production through glycolysis. This is because HK2 serves as the initial rate-limiting enzyme in the glycolysis pathway. Due to 3-BP treatment, severe energy depletion occurs, leading to cell death, which is supported by the upregulation of cleaved Caspase3. The increase in cleaved Caspase3 is a very well-known marker for apoptosis. The highly expressed cleaved Caspase3 in a 3-BP-treated tumor demonstrated that in the 3-BP group, a tumor-suppressing effect and tumor cell death occur through the induction of apoptosis.

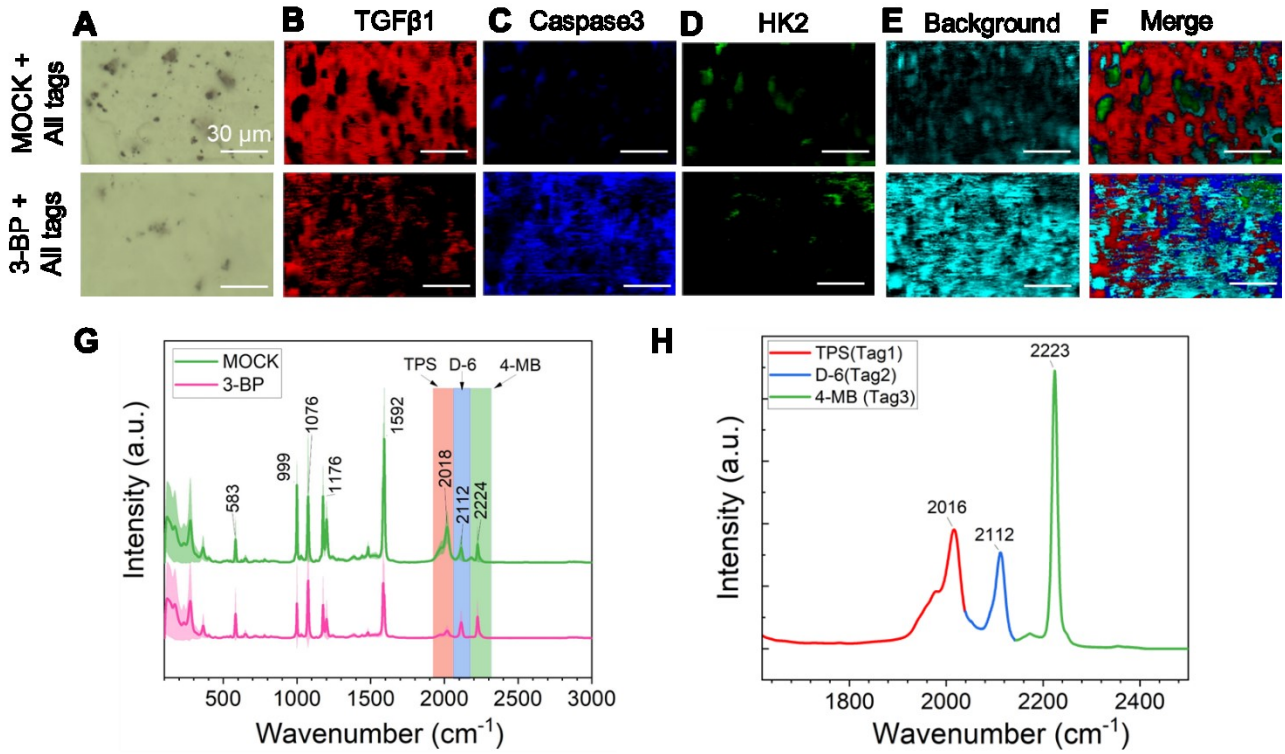

Figure 5. Multiplexed profiling of TGFβ1, Caspase3, and HK2 expression in the subcutaneous tissue from tumor model of pancreatic cancer with and without 3-BP treatment. **(A-F)** Representative mapping data comparing brightfield and SERS images of pancreatic tumors treated with saline (MOCK) or drug (3-BP). **(A)** Brightfield images of tissues treated with a mixture of all three tags: TGFβ1 & TPS (tag1), Caspase3 & D-6 (tag2), and HK2 & 4-MB (tag3). The corresponding SERS images of **(B)** tag1, **(C)** tag2, **(D)** tag3, **(E)** background, and **(F)** merged images are shown for both the MOCK (n = 49,029 spectra) and 3-BP (n = 47,775 spectra) groups. The spatial resolution of these images is 0.5 μm. **(G)** The comparison of Raman spectra of tissues containing all three tags is shown for the MOCK (green) and 3-BP (pink) groups. The shaded color on the spectra shows the standard deviation. The characteristic peak of TPS (2018 cm^{-1}), D-6 (2112 cm^{-1}), and 4-MB (2224 cm^{-1}) are shown. **(H)** Extracted Raman spectrum for each SERS tag identified

automatically after analyzing the Raman mapping images using empty modeling statistical method. The scale bar represents 30 μm.

2.4. Second Harmonic Generation (SHG) imaging

We studied the collagen content in the MOCK and 3-BP groups to investigate the tumor-associated microenvironments (TAMs) before and after the drug treatment. Extracellular matrix (ECM), capillaries, activated fibroblasts, immune cells, and basement membrane comprise the tumor stroma surrounding pancreatic cancer cells.[39] ECM plays a significant role during cancer progression since its physical properties can affect tumor stroma and protect tumor cells.[40]

ECM is split into two groups, basement membrane (BM) and interstitial membrane (IM), comprising different types of collagens.[40-41] Fibroblasts, cancer-associated fibroblasts (CAFs), and tumor-associated fibroblasts (TAFs) are stimulated by ECM remodeling and deposition during tumor invasion and progression.[39-40] Fibroblasts synthesize and form various collagens and work as mediators for tissue remodeling.[42] Once tumor initiation and progression happen, tumors behave similarly to wounds, responding to cancer fibrosis. Studies showed reactive stroma contains a high number of fibroblasts leading to collagen deposition around the tumor, while the normal ones have a minimal number.[43] To probe the expression level of collagens in MOCK and 3-BP treated tumor tissues, we performed SHG to calculate the level of collagen. In addition, to validate our SHG results, we performed picrosirius red and polarized light microscopy imaging as useful tools providing information about collagen.[44] The representative Picrosirius red image (**Figure 6A**) showed that the number of fibrotic collagen fibers (red color) was reduced after treatment in the 3-BP treated group compared to the MOCK group. The corresponding SHG images in (**Figures 6E – 6G)** revealed that the expression level of fibrotic collagens declined after treatment, which agrees with the polarization light microscope results (**Figure 6B**). Calculation of pixel intensity of picrosirius red images using ImageJ also showed a significant increase in the level of cytoplasm (yellow color) and a decrease in the level of muscle fiber (pink color) in 3BP treated tissues compared to the MOCK tissues (**Figures 6C** and **6D**).

Furthermore, a comparison of collagen levels in MOCK and 3-BP treated tissues calculated from the SHG images displayed a significant decrease ($P < 0.001$) in collagen expression after treatment in the 3-BP treated group (**Figure 6I**). However, the elastin level remained similar (**Figure 6H**). Ohlund et al. found highly expressed collagen type I after pancreatic cancer cell progression.[45] To understand the remodeling of TAMs after the 3-BP treatment, we also probed the metabolic alterations at the cellular level.[46] According to the Warburg effect, the ATP generation through oxidative phosphorylation in cancer cells turns to the aerobic glycolysis pathway.[47] Imaging two important metabolic coenzymes, reduced nicotinamide adenine dinucleotide (NADH) and oxidized flavin adenine dinucleotide (FAD), can determine the metabolic states of the cells.[48] Using the SHG and two-photon microscopy images, we calculated the redox ratio ($\frac{FAD}{FAD+NADH}$) in MOCK vs 3-BP treated tumor tissues. The redox ratio of the drug treated tissue, 3-BP group, showed significant increase ($P < 0.001$) in the redox ratio compared to the untreated tissue, MOCK group (**Figure 6J**). Varone et al. [48a] reported that a shift in metabolism from glycolysis to oxidative phosphorylation is responsible for an increase in the redox ratio.

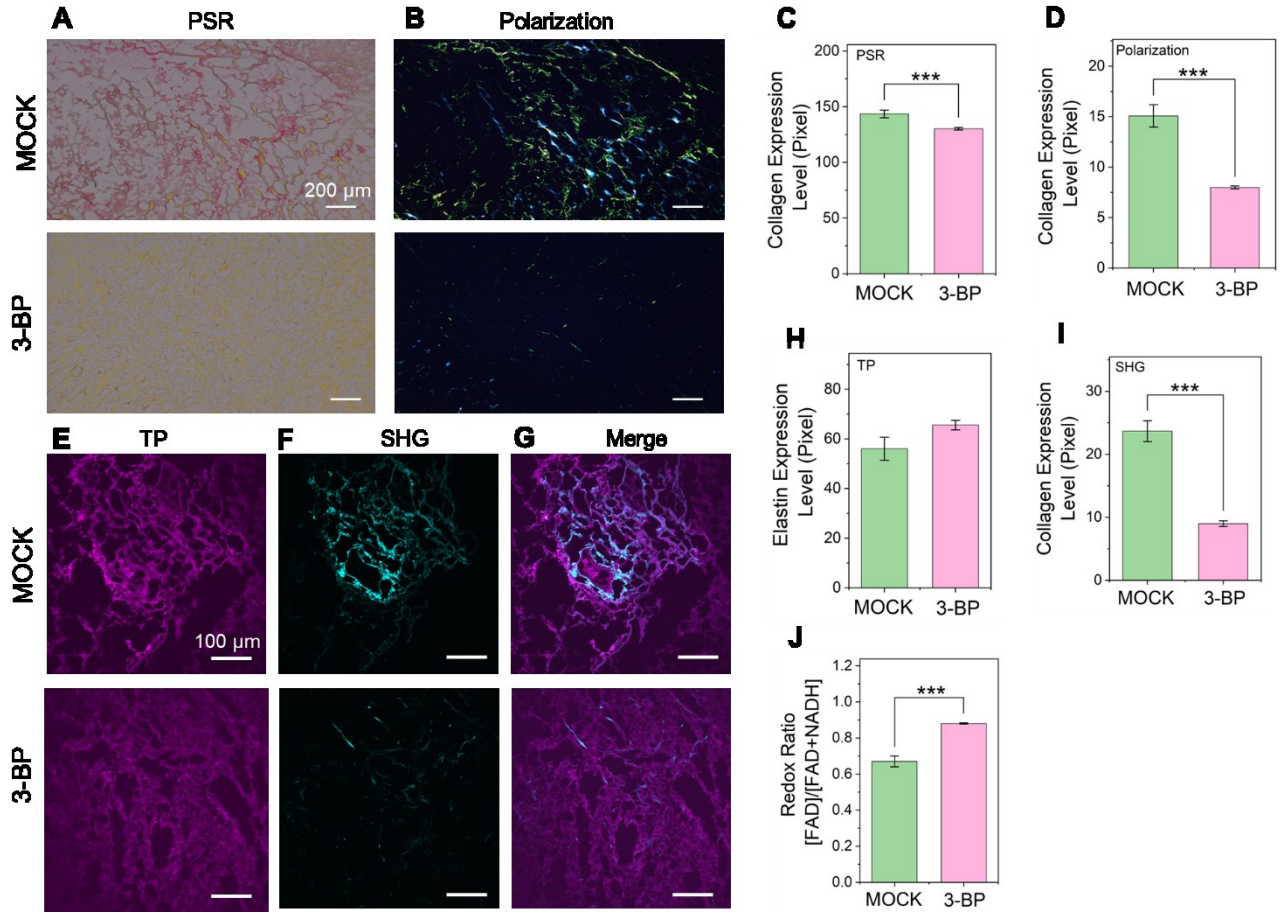

Figure 6. Comparison of the collagen expression level in the subcutaneous tissue from tumor model of pancreatic cancer before and after 3-BP treatment using multiphoton microscopy. Representative images showing the comparison of the **(A)** brightfield and **(B)** polarization images before (MOCK) and after (3-BP) 3-BP treatment of the tumor. The tissues are stained with picrosirius red (PSR). Quantification of collagen expression level using **(C)** PSR staining and **(D)** polarization images of MOCK and 3-BP tissues. Label-free metabolic imaging of MOCK and 3-BP tissues showing endogenous **(E)** two-photon fluorescence (TP), **(F)** second harmonic generation (SHG), and **(G)** merged microscopy images. The **(H)** elastin and (I) collagen levels are quantified from the TP and SHG images, respectively. **(J)** Comparison showing the quantification of redox ratio [FAD/(FAD+NADH)] in MOCK and 3-BP tissues. FAD level was derived from the TP images, whereas the NADH level was derived from the SHG images. Statistical significance was measured using a two-tailed Student's paired t-test with n=30 for each group. *P<0.05, **P<0.01, ***P<0.001; ns = not significant.

2. 5. Fluorescence Lifetime Imaging

FLIM has emerged as a promising diagnostic tool for tumor and drug treatment, owing to its ability to detect metabolic markers such as NADH and FAD.[49] **Figure 7A** shows the FLIM image of the pancreatic cancer tissue (MOCK) and drug-treated pancreatic cancer (3-BP). In the pseudo-colored images, the red color corresponds to a higher lifetime. **Figure 7B** shows the fluorescence lifetime decay curves for the MOCK (blue) and 3-BP treated (pink) samples. The figure demonstrates a slower radiative decay process for 3-BP than for MOCK samples. **Figure 7E** compares the distribution of τ_1 and τ_2 for MOCK and 3-BP treated group; here, the intensity is fitted with the function: $I(t) = A_1 \exp(-t/\tau_1) + A_2 \exp(-t/\tau_2)$ and τ_1 corresponds to fast components and τ_2 corresponds to the slow component of the lifetime, and A_1 and A_2 correspond to the amplitude of the fast and slow decay components, respectively. 3-BP showed higher τ_1 and τ_2 compared to MOCK **(Figure 7E)**. This is also confirmed by comparing the mean lifetime of these two groups (**Figure 7D**). The multicomponent nature of the lifetime is confirmed by the phasor plot in **Figure 7C**. The phasor plot is widely used to illustrate various free/bound protein NAD(P)H ratios that reveal changes in cell metabolism under particular circumstances.[49] An increased shift toward oxidative phosphorylation (OXPHOS) (3-BP treated group) from glycolysis (MOCK group) leads the phasor data toward the left side of the phasor plot (bound NAD(P)H leads to a higher lifetime).[50] The amplitude ratio (A_1/A_2) is shown in **Figure 7F**. The amplitude A_1 generally signifies unbound NAD(P)H, and A_2 signifies bound NAD(P)H. A higher amount of unbound NAD(P)H shows in cancer tissues and illustrates the glycolytic process. Remarkably, in our experiments, the A_1/A_2 ratio decreased after 3-BP treatment in the 3-BP treated group, indicating a decrease in glycolysis. Heaster et al.[51] showed that tumor-associated macrophages have a shorter mean lifetime (τ_m) than dermal macrophages as a result of alterations in NAD(P)H and FAD protein-binding activities.

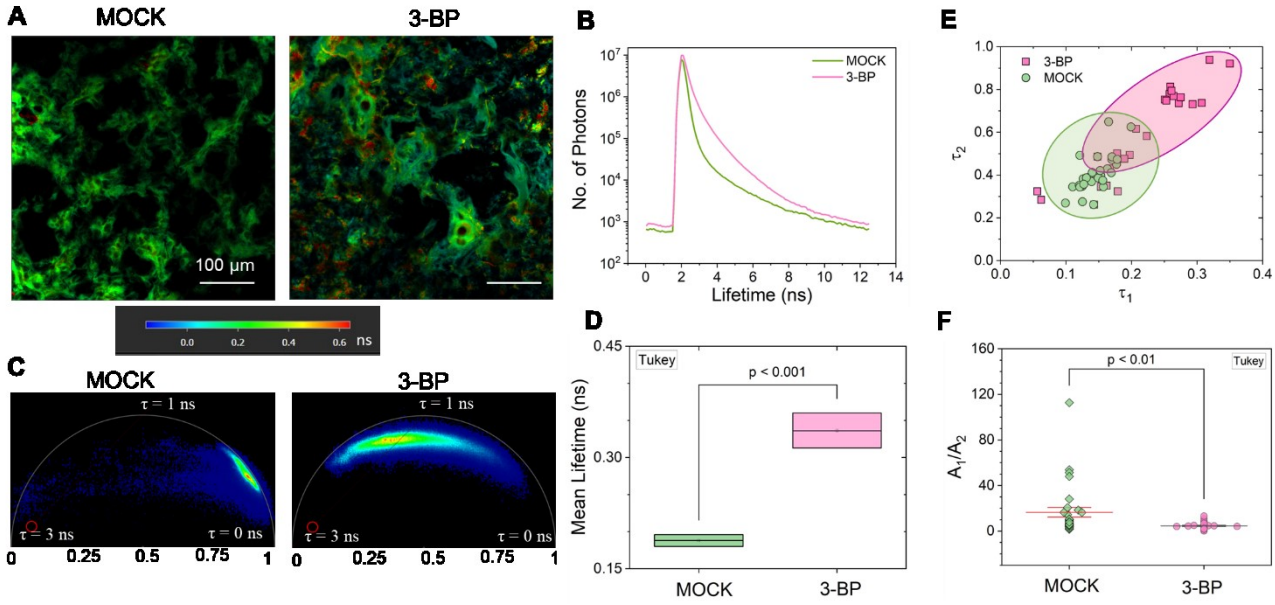

Figure 7. Mapping metabolic changes in the subcutaneous tissue from tumor model of pancreatic cancer after 3-BP treatment. Fluorescence lifetime imaging microscopy (FLIM) results of **(A)** MOCK and 3-BP sample. **(B)** Comparison of mean lifetime spectra for MOCK and 3-BP. The 3-BP group shows a slower decay rate signifying a larger fluorescence lifetime. **(C)** The phasor plot for the MOCK and 3-BP groups shows that the lifetimes are multicomponent. **(D)** Comparison of the mean lifetime for MOCK and 3-BP. **(E)** Distribution of faster (τ_1) and slower (τ_2) decay components of the lifetime for the 3-BP (pink) and MOCK (blue) samples. **(F)** Comparison of the ratio of the amplitude for the faster (A_1) and slower (A_2) decay components of the lifetime for the 3-BP (pink) and MOCK (blue) samples.

Because both NADH and FAD lifetime was increased, the lifetime of 3-BP treated pancreatic tumor samples in our investigation was consistently higher than that of control tumor (untreated) samples. Earlier studies that employed cell lines from metastatic melanoma revealed that the average lifetime of NADH was greater in non-metastatic cells compared to their metastatic counterparts. Specifically, the average lifetime of NADH in noncancerous cells was found to be between 1.4 to 1.9 nanoseconds, while in malignant cells, it ranged between 0.5 to 0.85 nanoseconds.[52] Experiments using human breast cancer cells demonstrated that hypoxia reduces the protein-bound and free NADH lifetime.[53] Skala et al. used two-photon excited FLIM to observe NADH and FAD in vivo in an oral cancer model, finding a significant decrease in the lifetime with increasing malignancy grade.[54] According to a separate study by Skala et al., the

shift from oxidative phosphorylation (OXPHOS) to glycolysis led to a decrease in the fluorescence lifetime of protein-bound NADH.[55] Wang et al. used $CoCl_2$ to inhibit OXPHOS and 3-BP to inhibit glycolysis in human lung epithelial cells (BEAS-2B).[56] Similar to our results, the study showed an increase in fluorescence lifetime compared to the control after the 3-BP treatment. This was due to the rise in FAD and NADH lifetime and inhibition of glycolysis. Our findings from data on the pancreatic tumor model are in line with the latest FLIM investigations in these in vitro or in vivo models.

2.6. Lipidomics analysis

To understand the changes in the lipidomic profile of tissue after 3-BP treatment, we performed an untargeted LC-MS analysis. About 301 distinct lipid species were found using the LC-MS analysis. The results revealed lipid species profiles in MOCK samples were altered after treatment with 3-BP in treated samples. As can be seen in the cumulative lipid composition analysis in (**Figure 8A)**, the MOCK sample has higher lipid compositions in comparison to 3-BP treated samples. Although lipids can boost pancreatic cancer cell growth, fatty acids *de novo* synthesis can be triggered by tumors for the rapid proliferation of cells.[57] The volcano plot of these species can be seen in (**Figure 8B**) with upregulated (red color) and downregulated (blue color) lipid species in 3-BP treated group compared to MOCK. A threshold of 2.0 for fold change and 0.05 for P-value was established. The volcano plot integrates fold change (FC) analysis and t-test into a single graph. We found that 33 lipid species were significantly upregulated, and 25 species were significantly downregulated in the 3-BP treated group compared to the MOCK group. **Figure 8E** shows Heat map clustering analysis for these upregulated and down-regulated lipids for each class of lipid species. The cumulative LysoDGTS and MGDG groups significantly decreased after 3-BP treatment compared to MOCK. TG was significantly elevated in the 3-BP treated group compared to the MOCK group. The treated (3-BP) and untreated (MOCK) pancreatic tumor samples were readily differentiated using PCA based on lipidomics analysis (**Figure 8D**). The distribution of the two groups' lipid metabolisms in different areas suggests that each group's lipid metabolism has its distinct features. The samples all fell within Hotelling's T Squared Ellipse's 95% confidence interval.

PCA analysis (**Figure 8D**) for the 3-BP treated and MOCK samples shows that the two data sets are significantly distinct due to the profile alteration in lipid species.

The plotted hierarchically clustered heat map (**Figure 8C**) analysis shows the upregulated (red) and downregulated (blue) lipid species in 3-BP treated and MOCK groups. The analysis categorized via Variable Importance in Projection (VIP) scores (shown in **Figure 8H**) indicates a clear difference in lipid species for each group among MOCK and 3-BPsamples. **Figure 8H** shows that in 3-BP samples, lipids subspecies including LysoDGTS (21:7), MG (19:8), PC (16:2), MGDG (18:5), TG (22:5), MG (18:8), PC (12:5), CL (24:2), DG (24:7), MG (27:10), MG (8:3), PC (17:2), DG (7:4), LysoDGTS (22:10), TG (27:9), DG (25:10), LysoDGTS (17:8), MGDG (17:2), DGTS (14:3), PC (27:4), MG (29:4), MG (10:1) are significantly upregulated, while MG (19:3), MGDG (18:3), MGDG (19:2) lipid species are shown to be downregulated. **Figures 8F** and **8G** show significant downregulation of cumulative LysoDGTS ($P<0.05$) and MGDG ($P<0.01$) in 3-BP samples after treatment. The level of LysoDGTS is positively correlated with the level of Apolipoprotein A1 (ApoA1).[58] ApoA1 is shown to have antitumor properties in pancreatic and other cancers.[59] Although, estrogen receptor (ER) positive breast cancer tissue showed that increased apoA1 levels contributed to treatment resistance.[60] It was found that apoA1 level increases glycolysis.[61] Our study found that the cumulative LysoDGTS decreased with 3-BP treatment, which could reduce the apoA1 level and the glycolysis. The reduction in glycolysis will reduce the glucose oxidation rate and the proliferation of cancer cells. Thus, our lipidomic study potentially links the lipid metabolism pathway in 3-BP treated tissues.

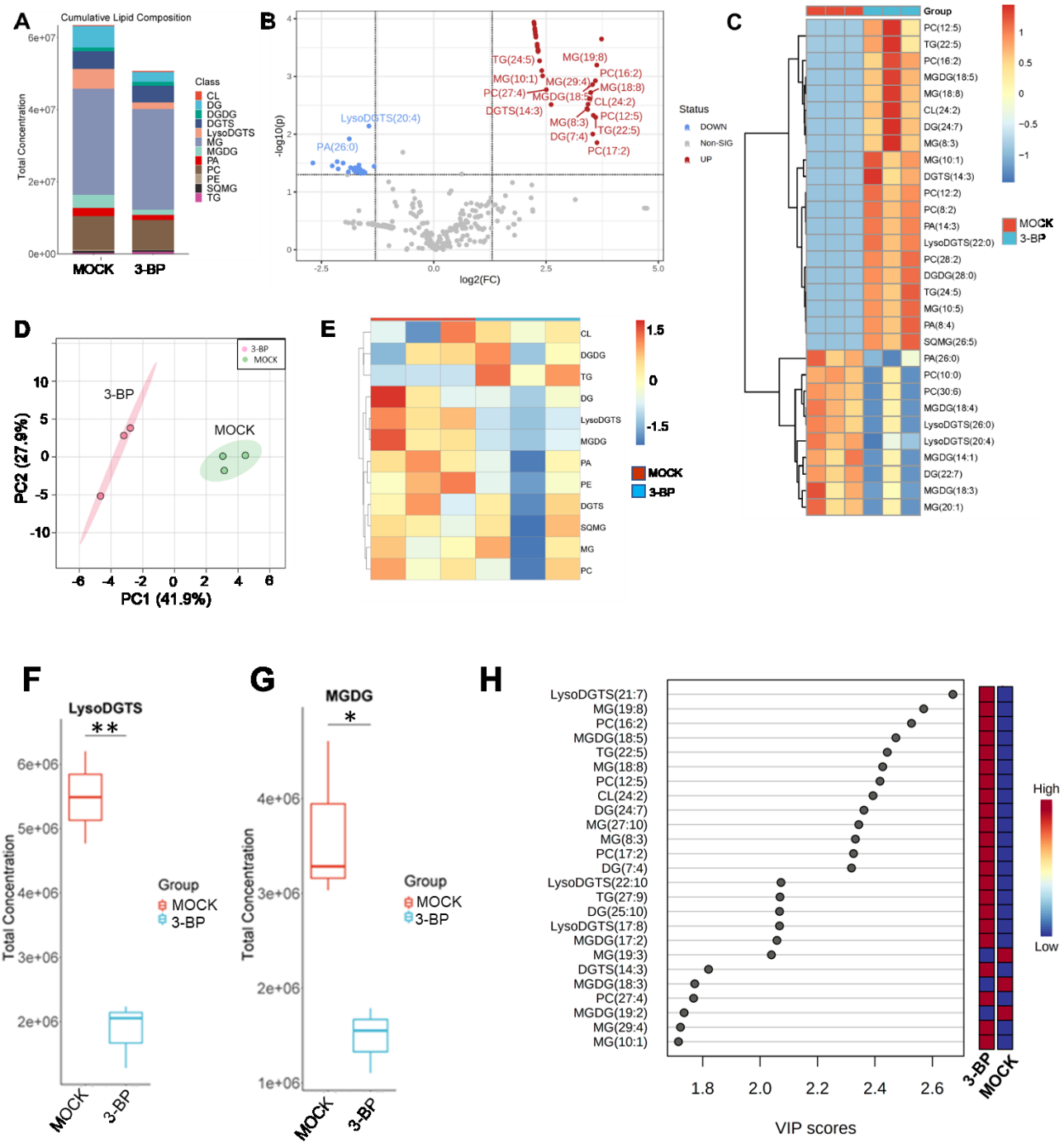

Figure 8. Profiling lipidomic changes in the subcutaneous tissue from tumor model of pancreatic cancer after 3-BP treatment. **(A)** Comparison of the histogram of cumulative lipid composition between MOCK and 3-BP groups showing a decrease in lipids after treatment (3-BP). **(B)** Volcano plot showing the upregulated (red) and downregulated (blue) lipid species in the 3-BP group compared to the MOCK group. **(C)** Hierarchically clustered heat maps show each group's lipid species change. **(D)** PCA score plot of the 3-BP and MOCK lipidomic datasets. **(E)** Heat map showing the difference in the alteration of each lipid

class. **(F)** LysoDGTS and **(G)** MGDG were significantly downregulated in the 3-BP group compared to the MOCK group. **(H)** Plot showing the top 25 lipid species with Variable Importance in Projection (VIP) scores > 1.8 obtained using Partial Least Squares Discriminant Analysis (PLS-DA). The red color box in a particular group indicates that specific species is significantly upregulated, and the blue color box indicates the related species is significantly downregulated.

We further analyzed the Raman images of the tissues by the Direct Classical Least Squares (DCLS) method[62] to profile lipid changes on the surface of tissues before and after treatment. The DCLS method is proper when we have a reference spectrum of the component we are profiling: lipids spectra. **Figure 9A** represents merged images of two lipid species for MOCK and 3-BP tissues. The corresponding Raman maps show a higher level of expression for PC, DHA, and LA in MOCK tissues, while TG, CL, Ch, AA, and OA is highly expressed in the 3-BP tissues after treatment. The corresponding effect size comparison showed a higher effect size for TG, PA, Ch, CL, AA, and OA in the 3-BP treated group compared to the control group **(Figure 9B)**. The corresponding plots of lipid scores are presented for the MOCK and 3-BP groups (**Figure 9C and 9D)**. According to the plots, TG, CL, Ch, AA, and OA increased, while PC, DHA, and LA decreased after treatment with 3-BP. This result is consistent with the lipidomics data.

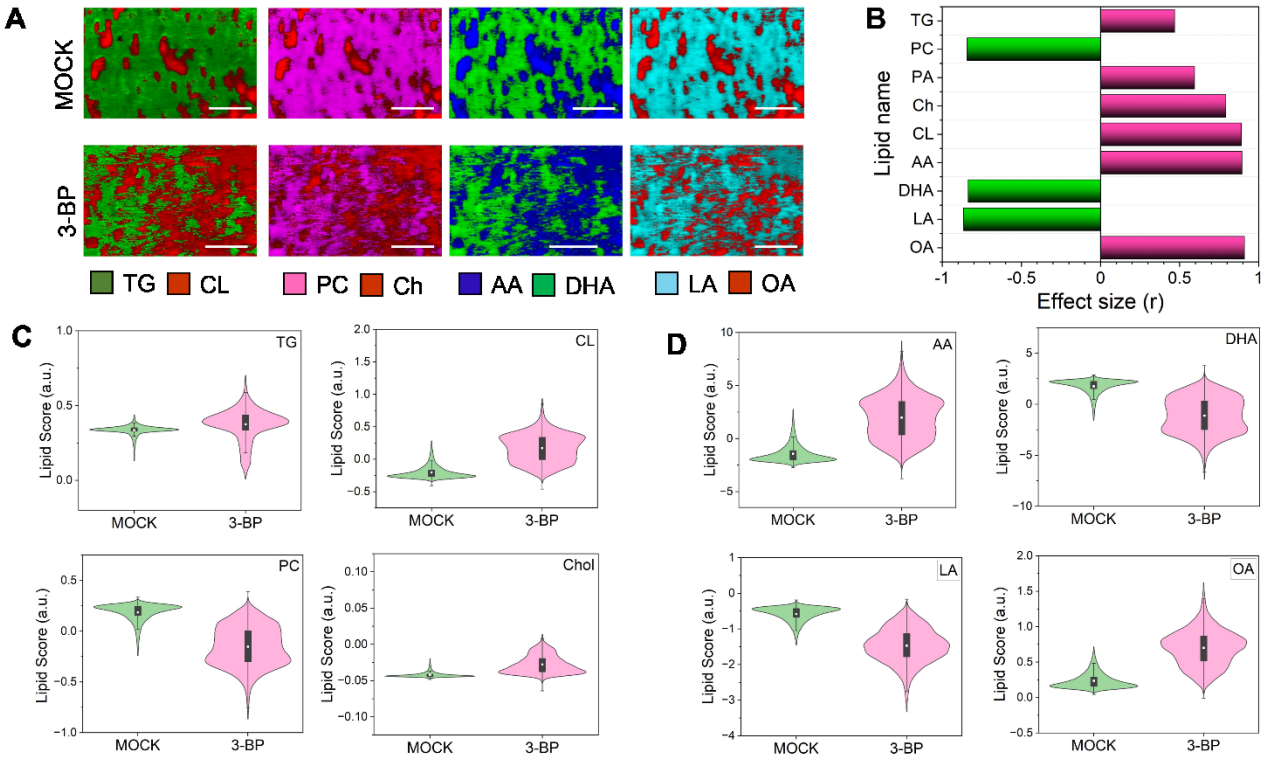

Figure 9. Representative Direct Classical Least Squares (DCLS)-based Raman mapping images comparing profile changes of various lipids expressed on the surface of tissues between MOCK and 3-BP group. **(A)** Merged images showing profile changes of Triglyceride (TG, green) and Cardiolipin (CL, red), Phosphatidyl Choline (PC, pink) and Cholesterol (Ch, red), Arachidonic Acid (AA, blue), and Docosahexaenoic Acid (DHA, green), Linoleic Acid (LA, cyan), and Oleic Acid (OA, red). **(B)** Comparison of the effect size of lipids calculated using Mann-Whitney U statistic and rank-biserial correlation. The corresponding Violin plots comparing each lipid score extracted from the Raman mapped images of MOCK and 3-BP tissues are shown for **(C)** TG, CL, PC, and Ch. **(D)** Lipid scores are plotted for AA, DHA, LA, and OA.

To further confirm the association of lipid metabolism with 3-BP treatment, we performed pathway analysis using the lipidomics data. **Figure 10A** shows the pathway enrichment results of the lipid-related genes in terms of the clusters. Cluster C2 is shown to have a high enrich ratio. The most significantly enriched pathways are represented in the form of clusters. The enrichment analysis revealed that Cluster C2 had a high enrich ratio with various pathways, including alpha-linoleic acid metabolism, glycerolipid metabolism, linoleic acid metabolism, ether lipid metabolism, and glycerophospholipid metabolism. Furthermore, the glycerophospholipid

metabolism pathway had a higher gene count (as indicated in **Figure 10B**) within this cluster. The lipids network graph (**Figure 10C**) shows the involvement of PCs and DGs in promoting pancreatic cancer cell proliferation. Our results suggest that the lipid metabolism pathways play an essential role in remodeling the pancreatic cancer tissue microenvironment.

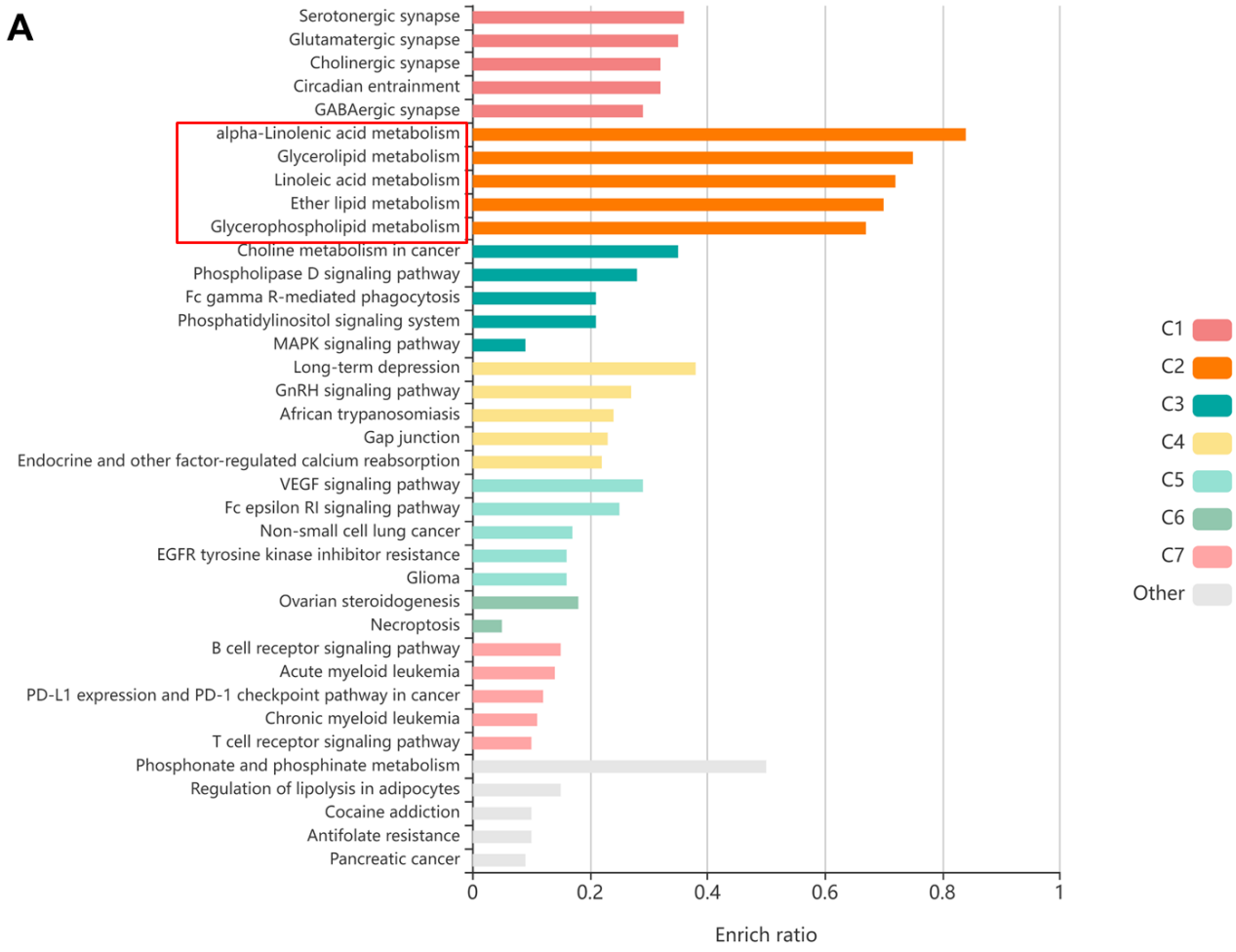

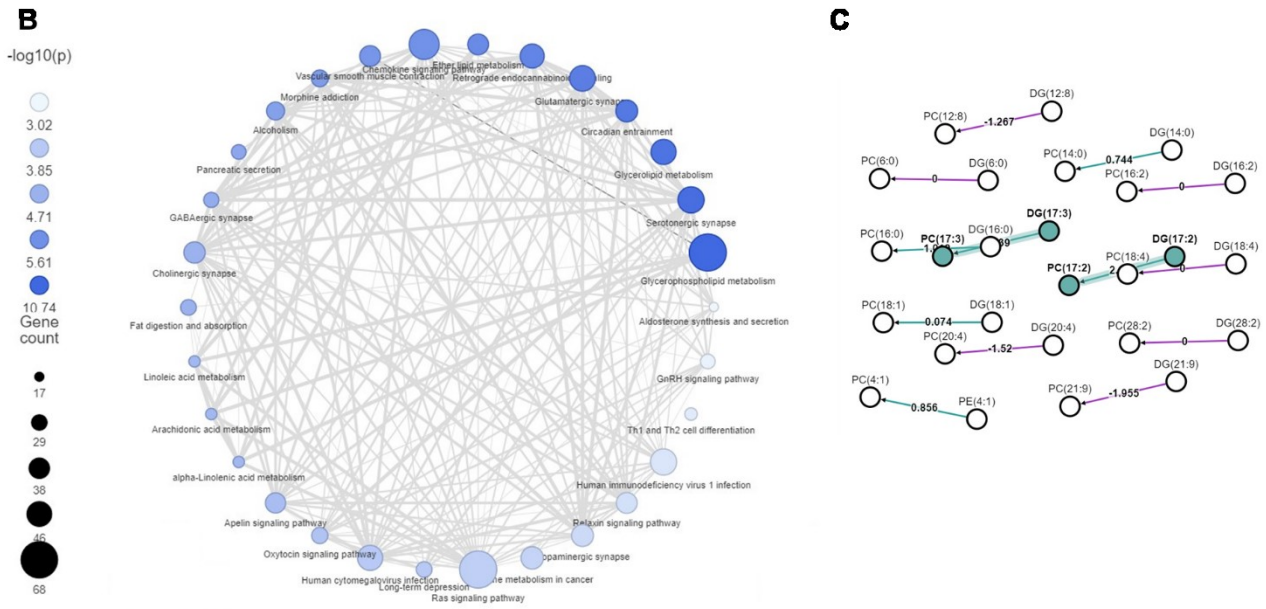

Figure 10. Lipid metabolism-related pathways due to 3-BP treatment**. (A)** Visualization of gene-list enrichment results. The bar plot of the *P*-value represents the different pathway analyses in terms of other clusters. **(B)** The enrichment network constructed using KEGG pathway analysis shows the significant pathways ($P < 0.05$) associated with differentially expressed lipid-related genes. The number of lipid-related genes engaged in the pathway is reflected by the size of the nodes, which are filled according to $-\log_{10}(P\text{-value})$. The line width shows the value of gene similarity between the pathways. **(C)** Lipid network graph generated using BioPAN for the 3-BP and MOCK group. Active lipids and active pathways are represented by green-shaded circles and shaded arrows, respectively. The green arrows denote reactions with a positive Z-score, and the purple arrows indicate reactions with negative Z-scores.

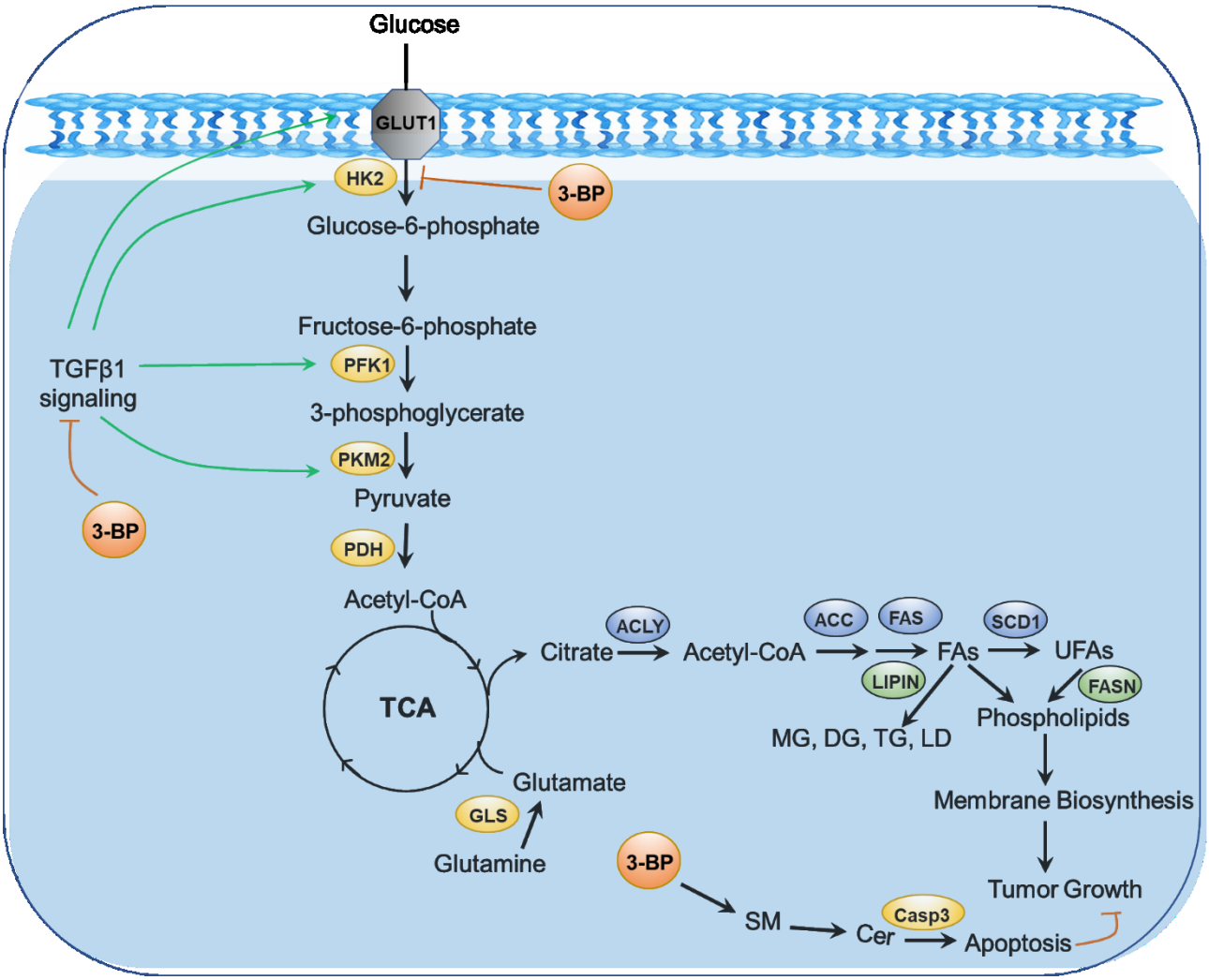

Figure 11. Schematic showing the mechanism of 3-BP and lipid metabolism in pancreatic cancer. Pancreatic cancer's lipid metabolism regulation involves enhanced glycolysis during TGFβ-induced signaling, resulting in high glycolytic activity in cancer cells. This increase in activity is due to the activation of glycolytic enzymes such as GLUT1, HK2, PFKFB3, PFK1, PKM2, and LDHA. In addition, the TGFβ signaling also inhibits PDK4, a negative regulator of PDH, which allows pyruvate to enter the TCA cycle.

Furthermore, the mitochondria convert glucose into fatty acids by producing citrate, which is subsequently transformed into acetyl-CoA by ACLY. Acetyl-CoA is regulated by ACC and FAS and is used for palmitate synthesis. Finally, the enzyme SCD1 facilitates the transformation of saturated fatty acids into monounsaturated fatty acids, which create phospholipids used in membrane construction and encourage the proliferation of tumors. In cancer cells, fatty acids are rapidly incorporated into triglycerides through either endogenous

synthesis or exogenous uptake, forming the core of lipid droplets. Hypoxia leads to an accumulation of these triglycerides and lipid droplets, which is associated with increased expression of LIPIN1, a key enzyme that transforms phosphatidic acid into diacylglycerol during TG synthesis. Treatment with 3-BP inhibits HK2 and TGFβ1, leading to decreased lipid synthesis and inducing apoptosis through the activation of Casp3.

3. Discussion

Pancreatic cancer is characterized by overexpression of HK2, which is associated with increased tumor growth (Roy et al, 2022)[3b], and dysregulated lipid metabolism. Notably, HK2 has been found to play a role in regulating lipid metabolism in pancreatic cancer cells.[63] HK2 has been shown to regulate the expression of key enzymes involved in lipid metabolism, including FASN (fatty acid synthase) and ACLY (ATP citrate lyase).[64] Additionally, HK2 is involved in regulating the AMPK (AMP-activated protein kinase) pathway, which plays a crucial role in regulating lipid metabolism and metabolic pathway.[65] Specifically, HK2 inhibition has been linked to the inhibition of AMPK activity, leading to increased killing of pancreatic cancer cells.[66] TGFβ1 signaling is also dysregulated in pancreatic cancer, with evidence suggesting a complex relationship with lipid metabolism.[67] Specifically, TGF-β1 has been shown to regulate the expression of several genes involved in lipid metabolism, including FASN (fatty acid synthase) [68] and SREBP-1c (sterol regulatory element-binding protein 1c).[69] 3-BP inhibits HK2, which reduces the GLUT1 activity and reduces lipid synthesis. This is evident by the cumulative lipid composition decrease after 3-BP treatment (**Figure 7A**).

Comparison of data showed strong correlation between Raman and LC-MS results [Pearson correlation coefficient R = 0.9935 as well as Raman and IHC results [Pearson correlation coefficient R = 0.9999 **Tables S8 and S9**. We found LysoDGTS (lysophosphatidylglycerol) decreased significantly ($P<0.001$) after 3-BP treatment (**Figure 7F**). LysoDGTS is a type of lysophospholipid implicated in several aspects of cancer biology, including tumor growth, metastasis, and chemotherapy resistance. One study found that LysoDGTS and DGTS levels were significantly higher in pancreatic cancer patients than in healthy controls.[70] Mutation of

p53 proteins leads to loss of tumor suppressive activities and may lead to additional oncogenic functions that allow cells to grow and survive.[71] 3-BP has been shown to degrade p53 to reduce the mutated p53.[12a] Previous study [72] showed p53 influenced lipid metabolism, and a reduction in p53 was accompanied by a reduction in lysophosphatidylglycerol (LysoDGTS) and other Lysophospholipids.

The data indicates how pancreatic cancer cells adjust to metabolic stress when faced with oncogenic signals such as LSL-KRAS^{G12D}. Lysophospholipid collection is a metabolic adaptation that cancer cells employ, providing an alternative nutrient source to sustain their growth and multiplication even in low-oxygen conditions.[73] Moreover, lysophospholipids are critical in biological processes as they function as signaling molecules.[74] Their quantities have been linked to cancer cell migration and invasion capabilities and overall regulatory mechanisms that maintain autocrine and paracrine signals, which are essential in the interactions between tumors and their microenvironments (TMEs).[75] The functions of lysophospholipids mentioned above rely on specific phospholipases regulated by intra- and extracellular stimuli.[76] Although the precise mechanisms by which LysoDGTS contributes to pancreatic cancer progression are not entirely understood, it has been proposed that LysoDGTS, along with different phospholipases C (PLC), may stimulate signaling pathways such as PI3K and AKT to enhance cancer cell proliferation and migration.[77]

4. Conclusions

Our study found that Raman spectroscopy combined with fluorescence lifetime imaging and second harmonic generation imaging effectively identifies lipid metabolism-related changes in the tumor microenvironment resulting from 3-BP treatment. The approach can be used for other drug treatment and disease systems. Future studies will explore its potential for monitoring response to primary tumor therapy and developing new cancer gene therapeutics. The study also demonstrated the capability of Raman spectroscopy for noninvasive assessment of tumor response to antiglycolytic therapy. However, future studies need to address some limitations, including evaluating combination immunotherapy and determining whether Raman

measurements can predict treatment response. The combination of SERS-based molecular imaging and lipidomics can potentially detect functional alterations in molecular markers during pancreatic cancer treatment with 3-BP. This approach could serve as a predictive biomarker for drug treatment response and resistance. SERS-based imaging of the tumor microenvironment with high spatial resolution could be used to anticipate the successful treatment of pancreatic cancer. By using a targeted Raman-enhanced molecular imaging approach in conjunction with multiphoton and lifetime imaging, multimodal-based imaging can effectively reveal the underlying tumor pathophysiology of the tumor microenvironment. Other studies have also shown the potential of lipidomics as a source of cancer biomarkers and therapeutic targets, and personalized approaches are necessary due to the heterogeneity of cancer. Further investigation is needed to understand lipidomes' underlying mechanisms and impact on cancer development and progression.

5. Experimental Methods

Materials. Pure gold nanospheres bare (Citrate) with a diameter of 60 nm were purchased from nanoComposix, USA. Dimethyl sulfoxide (DMSO) was purchased from Sigma, MO, USA. 4-Mercaptobenzonitril (4-MB) and tris(hydroxymethyl)aminomethane (Tris (HCl)) 1 M with pH: 8.5 were purchased from Biosynth, USA. Phosphate-Buffered Saline (PBS) was purchased from VWR, USA. Distilled water, dopamine hydrochloride, Dimethyl sulfoxide-d6 (D-6), and trimethyl(phenylethynyl)silane (TPS) were obtained from Sigma-Aldrich, USA. Hexokinase2 (HK2) and TGFβ1 were purchased from Santa Cruz Biotechnology, USA. Cleaved Caspase3 antibodies were obtained from Cell Signaling Technology, USA.

Preparation of SERS nanotags. 100 µL of gold nanoparticles (NPs) were functionalized with 2 µL of 100 mM Raman reporters (RRs) solutions prepared in DMSO and 98 µL of 0.1 mg/mL Dopamine in Tris buffer (10 mM, pH 8.5). After centrifugation of solutions for 15 min at 8000 rpm, the supernatant was extracted, and 100 µL of DI water was added to the precipitates. Again, solutions were centrifuged under the same condition to remove all the excess Dopamine and untagged RRs; and they were redispersed in 100 µL of DI water. For conjugation of antibodies, first, 4 µL of each antibody solution was added to each prepared solution and rotated vigorously

using a rotor (FisherScientific, USA) for 5 h and kept at 4 ºC for 18 h. After the completion of the reaction, 4 µL of 1 mg/mL of BSA solution was added and incubated at 37 ºC for 1 h. Then, solutions were centrifuged at 8000 rpm for 10 min to remove unconjugated antibodies, redispersed in PBS, and stored at 4 ºC for future use.

Physical characterization of SERS nanotags

Dynamic Light Scattering (DLS). Dynamic light scattering (DLS) measurements were carried out using a Malvern Zetasizer Nano ZS apparatus (Malvern Panalytical) equipped with a 4 mW He-Ne solid-state laser operating at 633 nm, and 25 °C. The backscattered light was collected at 173°.

TEM. Transmission Electron Microscopy (TEM) images were captured utilizing JEOL JEM-2010 TEM with an accelerating voltage of 200 kV.

UV-Vis spectrometry. The UV-vis spectra for the bare and conjugated nanoparticles were obtained using 6300 PC, VWR.

Raman spectroscopy experiments. Raman spectra of antibodies and nanotags without antibodies were captured using a Renishaw inVia Reflex Raman spectrometer, UK with 785 nm laser, the objective lens of 50X (long-working distance), (Leica, USA) with different powers depending on the type of samples, 1200 grating, and exposure time of 10 s using the extended mode.

Tissue experiments

Animal model. All the animal experiments were approved by IACUC, University of Maryland, Baltimore. This study involved the creation of a syngeneic subcutaneous mice model of pancreatic cancer, wherein mouse Panc-2 cancer cells were injected into the right flank of 8-week-old C57BL/6 female mice (n = 16). The animals were randomly assigned to two groups (n = 8 per group) and received either a 10-mg/kg 3-BP injection three times per week (every other day) for 30 days or a saline-only injection following the same schedule. Before tumor collection, animals were observed for an additional two weeks without being injected. Tissue samples were

collected, then treated with 4% paraformaldehyde solution, and kept at room temperature until further testing.

Tissue preparation for imaging. Both the control and treated tumor tissue were cryosectioned. Cryosections were prepared from frozen samples affixed to chucks with OCT compound and sectioned at 5 μm on a Leica CM1950 cryostat. Cryosections were picked up on Superfrost Plus Gold slides (Thermo Fisher, USA) and allowed to dry at room temperature overnight. Unstained cryosections were rehydrated in DI water before dehydration with ethanol and xylene. Finally, the coverslip was placed using Surgipath Sub-X mounting medium on a Leica ST5020/CV5030 Coverslipper (Leica Biosystems).

Raman imaging of tissues. All the tissue slices mounted on the stainless-steel metal slides were incubated with 100 μL of antibodies (anti-TGFβ1, anti-HK2, and anti-Caspase3) conjugated SERS nanotags for 1 h. After 1 h incubation, slices were thoroughly rinsed with PBS two times to remove nanotags adsorbed nonspecifically. Raman spectra of tag-stained tissues were obtained using a Renishaw inVia Reflex Raman spectrometer, UK, with 785 nm laser, Leica 63x water immersion objective, using various powers for each group of tissues, with a grating of 1200, and using exposure time = 10 s using extended mode. All the spectra were acquired in the wavenumber range of 100-3000 cm^{-1}. At least ten spectra were collected for each tissue sample. For taking SERS images of the tissues, mapping was done in SteamHR acquisition mode with a laser of 785 nm. Leica, 63x water immersion objective, was used with 10% power, 0.1 s exposure time, and step size of 0.5 μm, using static mode. To perform Raman spectroscopy and microscopy, all the tissues mounted on the metal slides were immersed in DI water, and the objective was then immersed in the water. The equipment was calibrated against Silicon (Si) peak at 520 cm^{-1}.

Raman map analysis – Empty Modeling. We used Empty modeling implemented in Renishaw's Windows®-based Raman Environment™ (WiRE) 4.4 software. Empty modeling's algorithm is an unsupervised technique that uses multivariate curve resolution alternating least squares (MCR-ALS). In the MCR-ALS method, the Raman spectrum is broken down into its component iteratively at each pixel of the Raman map. The fit is optimized at each time step till

the desired variance is achieved. The equation used is of the form $X = C*S^T + E$, where X = Raman spectra, C = concentration, S = component of the Raman spectra, and E = error; the output of the empty modeling analysis is C and S. The assumption in the MCR-ALS method is that the Raman spectrum at a pixel is a linear combination of pure component spectra. For example, the Raman spectrum at a pixel of a biological sample is a linear combination of the spectrum due to protein, DNA, lipid, and glucose molecule at that location. Empty modeling provides pseudo-quantitative information, such as the relative concentration profile of each component.

Histology. All fixed tissue sections were stained based on the hematoxylin-eosin (H&E) staining protocol for histopathological evaluation. Hematoxylin and eosin staining was done in Surgipath Sub-X mounting medium on a Leica ST5020/CV5030 autostainer (Leica Biosystems), and used SelecTech Hematoxylin 560, Eosin Phloxine 515, bluing, and define solutions (Leica Biosystems). Images were captured using NDP.view2 image viewing software, and all the images were analyzed with ImageJ.

Picrosirius red (PSR) staining and polarization microscopy. Dewaxed and rehydrated sections were stained with a picrosirius red stain kit (Polysciences, Inc., #24901) following manufacturer-specified procedures for FFPE and frozen tissue specimens. Collagen birefringence was visualized using a Leica DM6B microscope under polarized light at 10x/0.3 NA objective, and images were captured with a Leica DFC450 color CCD camera.

Immunohistochemistry imaging. Immunohistochemical detection of macrophages was performed on a Leica BOND-MAX auto-IHC platform running a modified "Protocol F" that included a 60 min primary antibody incubation step with a 1:1500 dilution of anti-Iba1 (Fujifilm Wako Chemicals, 019-19741) after a 20 min ER1 HIER step and used Leica's Polymer Refine Detection kit. Stained slides were dehydrated and coverslipped as above and allowed to dry entirely before scanning on a Hamamatsu Nanozoomer slide scanner using a 20x/0.8 NA dry objective. Images were captured using NDP.view2 image viewing software.

Liquid chromatography-mass spectrometry (LC-MS) experiments. First, all the tissues were lysed in a solution containing 250 µL of methanol (LC-MS grade) and homogenized with a Qsonica 500 until grinding all the chunks. Samples were kept under refrigeration or in ice throughout the sample preparation. Bradford protein quantification (Thermo Scientific) was performed to evaluate the protein concentration, and consequently, the tissue concentration was established using a 1:10 ratio of protein to tissue. Based on the protein amount measured, volumes containing 10 mg of equivalent tissue material were transferred to a new tube, 0.5 µg of Equisplash (Avanti Polar, Birmingham, AL) heavy labeled internal standard (IS) solution was added, and the sample vortexed for 1 min. Following the addition of the IS, 200 µL of LC-MS grade methanol was added, and the samples were vortexed for 1 min. We added 400 µL of HPLC grade chloroform to each tube, vortexed for 1 min, and kept it on ice for 10 min. This step was repeated three times. A portion (350 µL) of the organic layer was then transferred to a new tube and evaporated in a gentle stream of nitrogen. Samples were then reconstituted in 50 µL of 40% methanol solution containing 0.1% formic acid.
Agilent 1260 Infinity II quaternary liquid chromatograph coupled to an Agilent 6230 Electrospray Time-of-Flight mass spectrometer (Agilent, Santa Clara, CA) was used for LC-MS. Using a capillary voltage of 4000 V, samples were run. The fragment voltage was set to 125 V, and nitrogen was utilized as the drying gas, provided at a rate of 10 L/min at a temperature of 325 °C. 100-3000 m/z was the mass range that was employed. A binary mixture of mobile phases was employed for chromatographic separation using a gradient program utilizing an Agilent Poroshell 120 EC-C18 column (2.7 mm ID, 150 mm length, 2.7 µm pores, end-capped) at a fixed flow rate of 400 µL/min. The makeup of mobile stages was as follows: A = 0.1% formic acid in water and methanol (60:40, v/v), and B = methanol isopropanol (100:10, v/v). The gradient program was as follows: 0-5 min = 5% B, 5-30 min, 90% B, 30-35 min 90% B, 35-45 min 5% B. Each injection had a volume of 5 µL, and samples were run in positive mode. Utilizing the Qualitative Analysis Navigator module of the MassHunter Workstation, LC-MS samples were exported to mzData file format (Ver. B.08.00, Build 8.0.8208.0).

Multiphoton microscopy of tissues. The two-photon (TP) fluorescence and second harmonic generation (SHG) images of tissues were produced using a Spectra-Physics Mai-Tai femtosecond tunable pulsed near-IR laser (690 - 1040 nm) with a Leica SP5 resonant scanning

multiphoton confocal microscope. Images were acquired with a 25x water objective and at λ_{ex}=860 nm, 1024 x 1024 resolution using Leica application suit X (LAS X).

Fluorescence Lifetime Imaging Microscopy (FLIM) experiments. A Leica TCS SP8 confocal microscope with motorized DIC attachments was used to collect FLIM data. H&E-prepared slides were used to achieve the lifetime data. The Pancreatic cancer tissues were excited with a white light laser with an excitation wavelength of 561 nm and captured the emitted photons from 571 to 613 nm. We used a 63x/1.20 NA water immersion objective. Line repetitions and frame repetitions were set at 4. The pixel frame size was 1.14 µm x 1.14 µm for the FLIM images with a dwell time of 24.41 µs. With a 1.16 mm x 1.16 mm image size and 400 Hz tandem scanner speed, the corresponding frame rate shift was 0.024 s^{-1}. The fit for the decay rate was optimized after selecting multiple pixel places on the image of interest for finding an optimal χ^2 nearly close to 1.

Bioinformatics analysis. The data preprocessing and differential expression of lipids were performed using the LINT-Web server. The data cleaning and normalization were performed using the default settings. The sample clustering was also performed using the LINT-Web.[78] The differentially expressed lipids calculation was performed between 3-BP and MOCK groups. The 3-BP group was an experimental group, and the MOCK group was the control group. The differentially expressed lipids' pathway analysis and lipid gene enrichment were performed using the LipidSig web server [79] and BioPAN.[80]

Statistical analysis and data processing. Intelligent fitting of Renishaw's Wire 4.4 (Raman Software) was applied to perform baseline subtraction of all Raman spectra. Mapping data of tissues were analyzed using the empty modeling method. Plotting of all the Raman spectra was performed using OriginLab (OriginLab, Northampton, MA). All the quantifications of Raman images and other microscopy images were carried out using ImageJ. A two-tailed Student's *t*-test was used for the *P*-value calculation (statistical significance).

Supporting Information

Supporting Information is available from the Wiley Online Library or from the author.

Acknowledgments

Manas Ranjan Gartia (M.R.G.) was supported by National Science Foundation (NSF CAREER award number: 2045640). Research reported in this publication was supported by the National Institute of General Medical Sciences of the National Institutes of Health under award number R35GM150564. This project utilized the Cell Biology and Bioimaging Core that is supported in part by COBRE (P20 GM135002 & P20 GM103528) and NORC (P30 DK072476) center grants from the National Institutes of Health. Hem D Shukla was supported by NewG Lab pharma and Ko Discovery Inc.

References

[1] K. D. Miller, L. Nogueira, T. Devasia, A. B. Mariotto, K. R. Yabroff, A. Jemal, J. Kramer, R. L. Siegel, *CA: a cancer journal for clinicians* **2022**, 72, 409.

[2] a) H.-C. Yeh, C.-C. Su, Y.-H. Wu, C. H. Lee, B.-Y. Bao, W.-C. Cheng, S.-C. Wang, P.-L. Liu, C.-C. Chiu, C.-P. Chuu, *European Journal of Pharmacology* **2022**, 923, 174929; b) M. Ideno, S. Sasaki, M. Kobayashi, Y. Futagi, K. Narumi, K. Iseki, *Drug Metabolism and Pharmacokinetics* **2016**, 31, 67; c) E. Kwiatkowska, M. Wojtala, A. Gajewska, M. Soszyński, G. Bartosz, I. Sadowska-Bartosz, *Journal of bioenergetics and biomembranes* **2016**, 48, 23; d) D. Valenti, R. A. Vacca, L. de Bari, *Journal of bioenergetics and biomembranes* **2015**, 47, 493; e) X. Sun, G. Sun, Y. Huang, Y. Hao, X. Tang, N. Zhang, L. Zhao, R. Zhong, Y. Peng, *Biochemical Pharmacology* **2020**, 177, 113988; f) S. K. Gandham, M. Talekar, A. Singh, M. M. Amiji, *International journal of nanomedicine* **2015**, 10, 4405; g) S. L. Xian, W. Cao, X. D. Zhang, Y. F. Lu, *Oncology letters* **2015**, 9, 739.

[3] a) J. Chapiro, S. Sur, L. J. Savic, S. Ganapathy-Kanniappan, J. Reyes, R. Duran, S. C. Thiruganasambandam, C. R. Moats, M. Lin, W. Luo, *Clinical Cancer Research* **2014**, 20, 6406; b) S. Roy, T. Dukic, B. Bhandary, K. Tu, J. Molitoris, Y. Ko, H. Shukla, *American Journal of Cancer Research* **2022**, 12, 4977.

[4] a) G. C. Chu, A. C. Kimmelman, A. F. Hezel, R. A. DePinho, *Journal of cellular biochemistry* **2007**, 101, 887; b) D. Mahadevan, D. D. Von Hoff, *Molecular cancer therapeutics* **2007**, 6, 1186.

[5] A. S. Haka, K. E. Shafer-Peltier, M. Fitzmaurice, J. Crowe, R. R. Dasari, M. S. Feld, *Proceedings of the National Academy of Sciences* **2005**, 102, 12371.

[6] K. E. Shafer-Peltier, A. S. Haka, M. Fitzmaurice, J. Crowe, J. Myles, R. R. Dasari, M. S. Feld, *Journal of Raman Spectroscopy* **2002**, 33, 552.

[7] Z. Q. Wen, G. J. Thomas Jr, *Biopolymers: Original Research on Biomolecules* **1998**, 45, 247.

[8] W. R. Zipfel, R. M. Williams, R. Christie, A. Y. Nikitin, B. T. Hyman, W. W. Webb, *Proceedings of the National Academy of Sciences* **2003**, 100, 7075.

[9] a) N. Hay, *Nature Reviews Cancer* **2016**, 16, 635; b) D. DeWaal, V. Nogueira, A. R. Terry, K. C. Patra, S.-M. Jeon, G. Guzman, J. Au, C. P. Long, M. R. Antoniewicz, N. Hay, *Nature communications* **2018**, 9, 1.

[10] a) M. Anderson, R. Marayati, R. Moffitt, J. J. Yeh, *Oncotarget* **2017**, 8, 56081; b) K. C. Patra, N. Hay, *Oncotarget* **2013**, 4, 1862; c) K. C. Patra, Q. Wang, P. T. Bhaskar, L. Miller, Z. Wang, W. Wheaton, N. Chandel, M. Laakso, W. J. Muller, E. L. Allen, *Cancer cell* **2013**, 24, 213.

[11] P. Dell'Antone, *Medicinal Chemistry* **2009**, 5, 491.
[12] a) M. Petricciuolo, M. Davidescu, K. Fettucciari, L. Gatticchi, S. Brancorsini, R. Roberti, L. Corazzi, L. Macchioni, *Heliyon* **2020**, 6, e05741; b) M. Cal, I. Matyjaszczyk, I. Litwin, D. Augustyniak, R. Ogórek, Y. Ko, S. Ułaszewski, *Cells* **2020**, 9, 1161.
[13] a) L. K. Rotter, N. Berisha, H.-T. Hsu, K. H. Burns, C. Andreou, M. F. Kircher, *Nanotheranostics* **2022**, 6, 256; b) D. P. Bishop, N. Cole, T. Zhang, P. A. Doble, D. J. Hare, *Chemical Society Reviews* **2018**, 47, 3770.
[14] M. Angelo, S. C. Bendall, R. Finck, M. B. Hale, C. Hitzman, A. D. Borowsky, R. M. Levenson, J. B. Lowe, S. D. Liu, S. Zhao, *Nature medicine* **2014**, 20, 436.
[15] C. Giesen, H. A. Wang, D. Schapiro, N. Zivanovic, A. Jacobs, B. Hattendorf, P. J. Schüffler, D. Grolimund, J. M. Buhmann, S. Brandt, *Nature methods* **2014**, 11, 417.
[16] Y. Xianyu, J. Wu, Y. Chen, W. Zheng, M. Xie, X. Jiang, *Angewandte Chemie* **2018**, 130, 7625.
[17] W. Gao, T. Huang, H. Yuan, J. Yang, Q. Jin, C. Jia, G. Mao, J. Zhao, *Talanta* **2018**, 185, 229.
[18] a) A. Rao, D. Barkley, G. S. França, I. Yanai, *Nature* **2021**, 596, 211; b) R. Moncada, D. Barkley, F. Wagner, M. Chiodin, J. C. Devlin, M. Baron, C. H. Hajdu, D. M. Simeone, I. Yanai, *Nature biotechnology* **2020**, 38, 333; c) A. Andersson, L. Larsson, L. Stenbeck, F. Salmén, A. Ehinger, S. Z. Wu, G. Al-Eryani, D. Roden, A. Swarbrick, Å. Borg, *Nature communications* **2021**, 12, 1; d) E. Berglund, J. Maaskola, N. Schultz, S. Friedrich, M. Marklund, J. Bergenstråhle, F. Tarish, A. Tanoglidi, S. Vickovic, L. Larsson, *Nature communications* **2018**, 9, 1.
[19] a) L. Zhou, R. Wang, C. Yao, X. Li, C. Wang, X. Zhang, C. Xu, A. Zeng, D. Zhao, F. Zhang, *Nature communications* **2015**, 6, 1; b) Z. Liu, S. Tabakman, S. Sherlock, X. Li, Z. Chen, K. Jiang, S. Fan, H. Dai, *Nano research* **2010**, 3, 222.
[20] X.-S. Zheng, P. Hu, Y. Cui, C. Zong, J.-M. Feng, X. Wang, B. Ren, *Analytical chemistry* **2014**, 86, 12250.
[21] X.-M. Qian, S. M. Nie, *Chemical Society Reviews* **2008**, 37, 912.
[22] a) K. V. Kong, Z. Lam, W. K. O. Lau, W. K. Leong, M. Olivo, *Journal of the American Chemical Society* **2013**, 135, 18028; b) Y. Wang, B. Yan, L. Chen, *Chemical reviews* **2013**, 113, 1391.
[23] S. W. Joo, S. W. Han, K. Kim, *The Journal of Physical Chemistry B* **1999**, 103, 10831.
[24] a) L. A. Lane, X. Qian, S. Nie, *Chemical reviews* **2015**, 115, 10489; b) S. Lee, H. Chon, J. Lee, J. Ko, B. H. Chung, D. W. Lim, J. Choo, *Biosensors and Bioelectronics* **2014**, 51, 238.
[25] a) S. K. Paidi, J. Rodriguez Troncoso, P. Raj, P. Monterroso Diaz, J. D. Ivers, D. E. Lee, N. L. Avaritt, A. J. Gies, C. M. Quick, S. D. Byrum, *Cancer research* **2021**, 81, 5745; b) S. K. Paidi, J. R. Troncoso, M. G. Harper, Z. Liu, K. G. Nguyen, S. Ravindranathan, L. Rebello, D. E. Lee, J. D. Ivers, D. A. Zaharoff, *Theranostics* **2022**, 12, 5351; c) M. Hedegaard, C. Matthäus, S. Hassing, C. Krafft, M. Diem, J. Popp, *Theoretical Chemistry Accounts* **2011**, 130, 1249; d) N. Bergner, A. Medyukhina, K. D. Geiger, M. Kirsch, G. Schackert, C. Krafft, J. Popp, *Analytical and bioanalytical chemistry* **2013**, 405, 8719; e) C. Kallepitis, M. S. Bergholt, M. M. Mazo, V. Leonardo, S. C. Skaalure, S. A. Maynard, M. M. Stevens, *Nature communications* **2017**, 8, 14843.
[26] a) A. Y. You, M. S. Bergholt, J.-P. St-Pierre, W. Kit-Anan, I. J. Pence, A. H. Chester, M. H. Yacoub, S. Bertazzo, M. M. Stevens, *Science advances* **2017**, 3, e1701156; b) V. LaLone, A. Aizenshtadt, J. Goertz, F. S. Skottvoll, M. B. Mota, J. You, X. Zhao, H. E. Berg, J. Stokowiec, M. Yu, *Cell Reports Methods* **2023**.
[27] a) M. Li, J. Li, H. Di, H. Liu, D. Liu, *Analytical chemistry* **2017**, 89, 3532; b) H. Di, H. Liu, M. Li, J. Li, D. Liu, *Analytical chemistry* **2017**, 89, 5874; c) Y.-Q. Zhang, N. Kepčija, M. Kleinschrodt, K. Diller, S. Fischer, A. C. Papageorgiou, F. Allegretti, J. Björk, S. Klyatskaya, F. Klappenberger, *Nature communications* **2012**, 3, 1; d) C. r. Lee, S. J. Bae, M. s. Gong, K. Kim, S. W. Joo, *Journal of Raman Spectroscopy* **2002**, 33, 429; e) J. Wu, D. Liang, Q. Jin, J. Liu, M. Zheng, X. Duan, X. Tang,

Chemistry–A European Journal **2015**, 21, 12914; f) J. Ando, M. Asanuma, K. Dodo, H. Yamakoshi, S. Kawata, K. Fujita, M. Sodeoka, *Journal of the American Chemical Society* **2016**, 138, 13901.
[28] P. Maity, S. Takano, S. Yamazoe, T. Wakabayashi, T. Tsukuda, *Journal of the American Chemical Society* **2013**, 135, 9450.
[29] D. C. Kennedy, C. S. McKay, L.-l. Tay, Y. Rouleau, J. P. Pezacki, *Chemical Communications* **2011**, 47, 3156.
[30] a) J. Li, H. Liu, P. Rong, W. Zhou, X. Gao, D. Liu, *Nanoscale* **2018**, 10, 8292; b) H. Lee, S. M. Dellatore, W. M. Miller, P. B. Messersmith, *science* **2007**, 318, 426.
[31] B. K. Ahn, *Journal of the American Chemical Society* **2017**, 139, 10166.
[32] I. Badillo-Ramírez, J. M. Saniger, J. Popp, D. Cialla-May, *Physical Chemistry Chemical Physics* **2021**, 23, 12158.
[33] a) X. Qian, X.-H. Peng, D. O. Ansari, Q. Yin-Goen, G. Z. Chen, D. M. Shin, L. Yang, A. N. Young, M. D. Wang, S. Nie, *Nature biotechnology* **2008**, 26, 83; b) Y. Yin, Q. Li, S. Ma, H. Liu, B. Dong, J. Yang, D. Liu, *Analytical chemistry* **2017**, 89, 1551.
[34] a) H. Maehira, T. Miyake, H. Iida, A. Tokuda, H. Mori, D. Yasukawa, K.-i. Mukaisho, T. Shimizu, M. Tani, *Annals of surgical oncology* **2019**, 26, 4791; b) C. Han, T. Liu, R. Yin, *Biomarker Research* **2020**, 8, 1.
[35] H. D. Shukla, T. Dukic, S. Roy, B. Bhandary, A. Gerry, Y. Poirier, N. Lamichhane, J. Molitoris, F. Carrier, A. Banerjee, *Frontiers in Oncology* **2023**, 12, 1072774.
[36] a) S. F. Valilou, M. Keshavarz-Fathi, N. Silvestris, A. Argentiero, N. Rezaei, *Cytokine & growth factor reviews* **2018**, 39, 46; b) L. Bingle, N. Brown, C. E. Lewis, *The Journal of Pathology: A Journal of the Pathological Society of Great Britain and Ireland* **2002**, 196, 254.
[37] H. Wu, J. B. Xu, Y. L. He, J. J. Peng, X. H. Zhang, C. Q. CHEN, W. Li, S. R. Cai, *Journal of surgical oncology* **2012**, 106, 462.
[38] F. Pierezan, J. Mansell, A. Ambrus, A. R. Hoffmann, *Journal of comparative pathology* **2014**, 151, 347.
[39] R. Kalluri, *Nature Reviews Cancer* **2016**, 16, 582.
[40] N. I. Nissen, M. Karsdal, N. Willumsen, *Journal of Experimental & Clinical Cancer Research* **2019**, 38, 1.
[41] B. Piersma, M. Hayward, V. M. Weaver, *Biochimica et Biophysica Acta (BBA)-Reviews on Cancer* **2020**, 1873, 188356.
[42] S. Xu, H. Xu, W. Wang, S. Li, H. Li, T. Li, W. Zhang, X. Yu, L. Liu, *Journal of translational medicine* **2019**, 17, 1.
[43] R. Kalluri, M. Zeisberg, *Nature Reviews Cancer* **2006**, 6, 392.
[44] a) R. Lattouf, R. Younes, D. Lutomski, N. Naaman, G. Godeau, K. Senni, S. Changotade, *Journal of Histochemistry & Cytochemistry* **2014**, 62, 751; b) J. Liu, M. y. Xu, J. Wu, H. Zhang, L. Yang, D. x. Lun, Y. c. Hu, B. Liu, *Orthopaedic Surgery* **2021**, 13, 701.
[45] D. Öhlund, O. Franklin, E. Lundberg, C. Lundin, M. Sund, *BMC cancer* **2013**, 13, 1.
[46] S. Wu, Y. Huang, Q. Tang, Z. Li, H. Horng, J. Li, Z. Wu, Y. Chen, H. Li, *Biomedical Optics Express* **2018**, 9, 1375.
[47] a) R. A. Cairns, I. S. Harris, T. W. Mak, *Nature Reviews Cancer* **2011**, 11, 85; b) A. J. Walsh, R. S. Cook, H. C. Manning, D. J. Hicks, A. Lafontant, C. L. Arteaga, M. C. Skala, *Cancer research* **2013**, 73, 6164.
[48] a) A. Varone, J. Xylas, K. P. Quinn, D. Pouli, G. Sridharan, M. E. McLaughlin-Drubin, C. Alonzo, K. Lee, K. Münger, I. Georgakoudi, *Cancer research* **2014**, 74, 3067; b) N. Mehta, S. Shaik, A. Prasad, A. Chaichi, S. P. Sahu, Q. Liu, S. M. A. Hasan, E. Sheikh, F. Donnarumma, K. K. Murray, *Advanced Functional Materials* **2021**, 31, 2103955.
[49] Y. Ouyang, Y. Liu, Z. M. Wang, Z. Liu, M. Wu, *Nano-Micro Letters* **2021**, 13, 1.

[50] a) X. Wang, Y. Wang, Z. Zhang, M. Huang, Y. Fei, J. Ma, L. Mi, *Biomedical Optics Express* **2020**, 11, 1977; b) T. S. Blacker, Z. F. Mann, J. E. Gale, M. Ziegler, A. J. Bain, G. Szabadkai, M. R. Duchen, *Nature communications* **2014**, 5, 1.

[51] T. M. Heaster, A. R. Heaton, P. M. Sondel, M. C. Skala, *Frontiers in bioengineering and biotechnology* **2021**, 9, 644648.

[52] a) A. Pradhan, P. Pal, G. Durocher, L. Villeneuve, A. Balassy, F. Babai, L. Gaboury, L. Blanchard, *Journal of Photochemistry and Photobiology B: Biology* **1995**, 31, 101; b) K. Drozdowicz-Tomsia, A. G. Anwer, M. A. Cahill, K. N. Madlum, A. M. Maki, M. S. Baker, E. M. Goldys, *Journal of biomedical optics* **2014**, 19, 086016.

[53] D. K. Bird, L. Yan, K. M. Vrotsos, K. W. Eliceiri, E. M. Vaughan, P. J. Keely, J. G. White, N. Ramanujam, *Cancer research* **2005**, 65, 8766.

[54] M. C. Skala, K. M. Riching, A. Gendron-Fitzpatrick, J. Eickhoff, K. W. Eliceiri, J. G. White, N. Ramanujam, *Proceedings of the National Academy of Sciences* **2007**, 104, 19494.

[55] M. C. Skala, K. M. Riching, D. K. Bird, A. Gendron-Fitzpatrick, J. Eickhoff, K. W. Eliceiri, P. J. Keely, N. Ramanujam, *Journal of biomedical optics* **2007**, 12, 024014.

[56] M. Wang, F. Tang, X. Pan, L. Yao, X. Wang, Y. Jing, J. Ma, G. Wang, L. Mi, *BBA clinical* **2017**, 8, 7.

[57] D. Zhou, D. Mu, M. Cheng, Y. Dou, X. Zhang, Z. Feng, G. Qiu, H. Yu, Y. Chen, H. Xu, *Acta Cirúrgica Brasileira* **2020**, 35.

[58] A. Khattib, D. Atrahimovich, L. Dahli, J. Vaya, S. Khatib, *BioFactors* **2020**, 46, 146.

[59] a) Y. Zhang, L. Zheng, *Translational Cancer Research* **2020**, 9, 3712; b) J. Wu, C. Zhang, G. Zhang, Y. Wang, Z. Zhang, W. Su, J. Lyu, *Cellular Physiology and Biochemistry* **2018**, 51, 575; c) X. Liu, W. Zheng, W. Wang, H. Shen, L. Liu, W. Lou, X. Wang, P. Yang, *British journal of cancer* **2017**, 117, 1846; d) M. Ehmann, K. Felix, D. Hartmann, M. Schnölzer, M. Nees, S. Vorderwülbecke, R. Bogumil, M. W. Büchler, H. Friess, *Pancreas* **2007**, 34, 205; e) K. Georgila, D. Vyrla, E. Drakos, *Cancers* **2019**, 11, 1097.

[60] V. C. Hodgkinson, V. Agarwal, D. ELFadl, J. N. Fox, P. L. McManus, T. K. Mahapatra, P. J. Kneeshaw, P. J. Drew, M. J. Lind, L. Cawkwell, *Journal of proteomics* **2012**, 75, 2745.

[61] M. Lehti, E. Donelan, W. Abplanalp, O. Al-Massadi, K. M. Habegger, J. Weber, C. Ress, J. Mansfeld, S. Somvanshi, C. Trivedi, *Circulation* **2013**, 128, 2364.

[62] a) D. P. Kelley, A. Chaichi, A. Duplooy, D. Singh, M. R. Gartia, J. Francis, *Neurobiology of stress* **2022**, 20, 100476; b) A. Chaichi, S. M. A. Hasan, N. Mehta, F. Donnarumma, P. Ebenezer, K. K. Murray, J. Francis, M. R. Gartia, *Analyst* **2021**, 146, 170.

[63] a) S.-J. Wang, X.-D. Li, L.-P. Wu, P. Guo, L.-X. Feng, B. Li, *Journal of Cancer* **2021**, 12, 1144; b) H. Ogawa, H. Nagano, M. Konno, H. Eguchi, J. Koseki, K. Kawamoto, N. Nishida, H. Colvin, A. Tomokuni, Y. Tomimaru, *Molecular and clinical oncology* **2015**, 3, 563; c) F. Li, C. He, H. Yao, Y. Zhao, X. Ye, S. Zhou, J. Zou, Y. Li, J. Li, S. Chen, *Pharmacological Research* **2023**, 187, 106555.

[64] a) D. Guo, E. Hlavin Bell, P. Mischel, A. Chakravarti, *Current pharmaceutical design* **2014**, 20, 2619; b) J.-S. Moon, W.-J. Jin, J.-H. Kwak, H.-J. Kim, M.-J. Yun, J.-W. Kim, S. W. Park, K.-S. Kim, *Biochemical Journal* **2011**, 433, 225.

[65] a) Y. Angin, C. Beauloye, S. Horman, L. Bertrand, *AMP-Activated Protein Kinase* **2016**, 23; b) L. Xia, L. Oyang, J. Lin, S. Tan, Y. Han, N. Wu, P. Yi, L. Tang, Q. Pan, S. Rao, *Molecular cancer* **2021**, 20, 1; c) H. Xiang, R. Yang, J. Tu, Y. Xi, S. Yang, L. Lv, X. Zhai, Y. Zhu, D. Dong, X. Tao, *Biomedicine & Pharmacotherapy* **2023**, 157, 113992; d) B. Kim, J. Gwak, M. Kim, S. Yang, S. Hwang, S. Shin, J. H. Kim, J. Son, S. M. Jeong, *Cancer Gene Therapy* **2023**, 1.

[66] M. Hu, X. Chen, L. Ma, Y. Ma, Y. Li, H. Song, J. Xu, L. Zhou, X. Li, Y. Jiang, *Journal of Cancer* **2019**, 10, 1870.

[67] a) L. Gabitova-Cornell, A. Surumbayeva, S. Peri, J. Franco-Barraza, D. Restifo, N. Weitz, C. Ogier, A. R. Goldman, T. R. Hartman, R. Francescone, *Cancer Cell* **2020**, 38, 567; b) M. A. Mouti, S. Pauklin, *Molecular Therapy* **2021**, 29, 920.
[68] J. A. Menendez, A. Vazquez-Martin, F. J. Ortega, J. M. Fernandez-Real, *Clinical chemistry* **2009**, 55, 425.
[69] a) S. Kugel, S. R. Hingorani, *Cancer Cell* **2020**, 38, 443; b) A. O. Ogunleye, R. K. Nimmakayala, S. K. Batra, M. P. Ponnusamy, *Stem Cells* **2023**, sxad017.
[70] H. Xu, J. Sun, L. Zhou, Q.-C. Du, H.-Y. Zhu, Y. Chen, X.-Y. Wang, *World Journal of Clinical Cases* **2021**, 9, 10884.
[71] a) N. Rivlin, R. Brosh, M. Oren, V. Rotter, *Genes & cancer* **2011**, 2, 466; b) S. Weissmueller, E. Manchado, M. Saborowski, J. P. Morris IV, E. Wagenblast, C. A. Davis, S.-H. Moon, N. T. Pfister, D. F. Tschaharganeh, T. Kitzing, *Cell* **2014**, 157, 382.
[72] A. Butera, M. Roy, C. Zampieri, E. Mammarella, E. Panatta, G. Melino, A. D'Alessandro, I. Amelio, *Biology direct* **2022**, 17, 6.
[73] J. J. Kamphorst, J. R. Cross, J. Fan, E. De Stanchina, R. Mathew, E. P. White, C. B. Thompson, J. D. Rabinowitz, *Proceedings of the National Academy of Sciences* **2013**, 110, 8882.
[74] Y. Xu, *Cancers* **2018**, 10, 227.
[75] a) U. Ray, S. Roy Chowdhury, M. Vasudevan, K. Bankar, S. Roychoudhury, S. S. Roy, *Molecular oncology* **2017**, 11, 491; b) T. K. Phan, S. A. Williams, G. K. Bindra, F. T. Lay, I. K. H. Poon, M. D. Hulett, *Cell Death & Differentiation* **2019**, 26, 781.
[76] J. B. Park, C. S. Lee, J.-H. Jang, J. Ghim, Y.-J. Kim, S. You, D. Hwang, P.-G. Suh, S. H. Ryu, *Nature Reviews Cancer* **2012**, 12, 782.
[77] G. Hoxhaj, B. D. Manning, *Nature Reviews Cancer* **2020**, 20, 74.
[78] F. Li, J. Song, Y. Zhang, S. Wang, J. Wang, L. Lin, C. Yang, P. Li, H. J. S. M. Huang, **2021**, 5, 2100206.
[79] W.-J. Lin, P.-C. Shen, H.-C. Liu, Y.-C. Cho, M.-K. Hsu, I.-C. Lin, F.-H. Chen, J.-C. Yang, W.-L. Ma, W.-C. J. N. A. R. Cheng, **2021**, 49, W336.
[80] C. Gaud, B. C. Sousa, A. Nguyen, M. Fedorova, Z. Ni, V. B. O'Donnell, M. J. Wakelam, S. Andrews, A. F. J. F. Lopez-Clavijo, **2021**, 10.

Table of contents.

Elnaz Sheikh, Kirti Agrawal, Sanjit Roy, David Burk, Fabrizio Donnarumma, Young H. Ko, Praveen Kumar Guttula, Nrusingh C. Biswa*, Hem D. Shukla*, Manas Ranjan Gartia*

Multimodal Imaging of Pancreatic Cancer Microenvironment in Response to an Antiglycolytic Drug

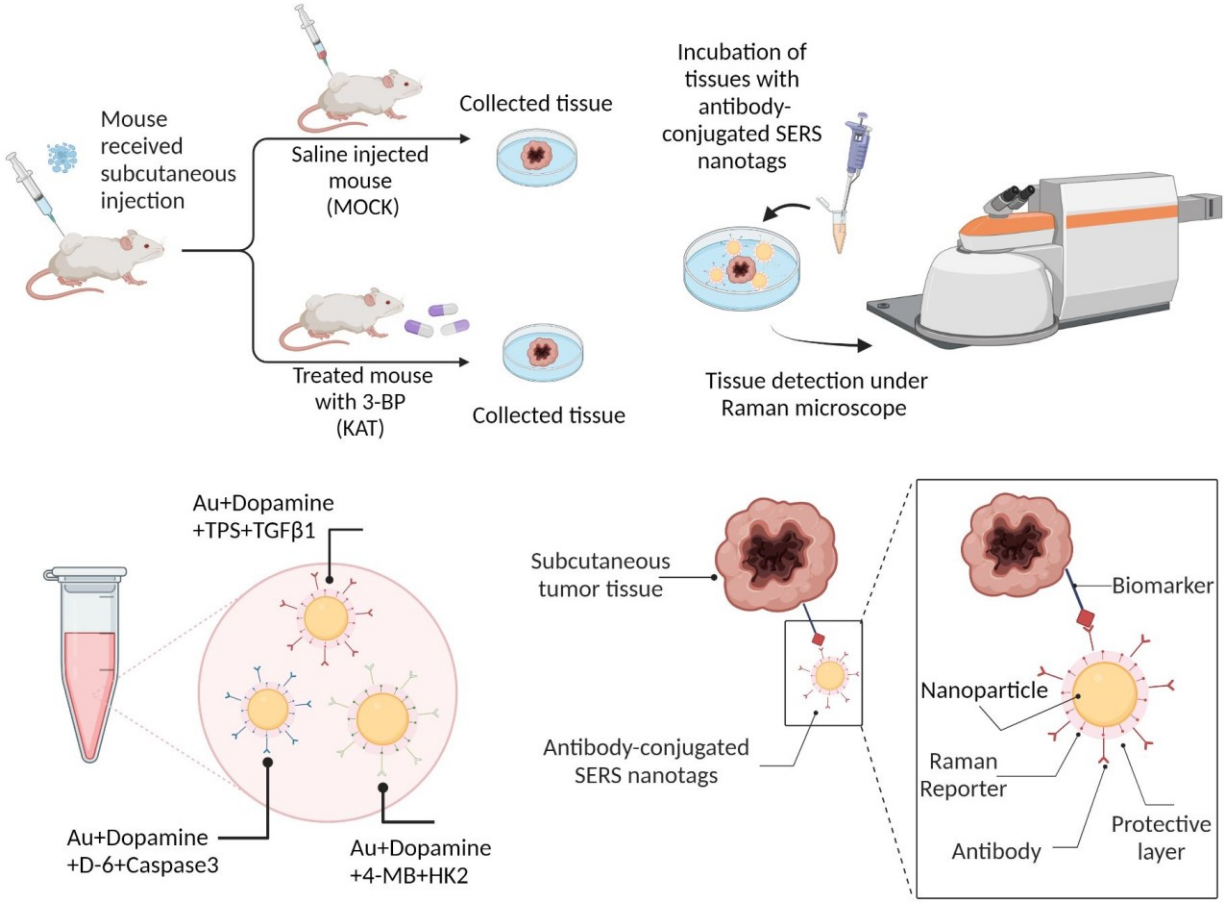

Simultaneous profiling of lipids, collagen, and proteins is challenging using a single immunohistochemistry marker. The rational design of surface-enhanced Raman spectroscopy (SERS) nanotags in the Raman-silent region helps us to perform spatial mapping of multiple proteins and lipids in the pancreatic tumor model after treatment.

Supporting Information

Multimodal Imaging of Pancreatic Cancer Microenvironment in Response to an Antiglycolytic Drug

Elnaz Sheikh, Kirti Agrawal, Sanjit Roy, David Burk, Fabrizio Donnarumma, Young H. Ko, Praveen Kumar Guttula, Nrusingh C. Biswa, Hem D. Shukla*, Manas Ranjan Gartia**

E. Sheikh, K. Agrawal, M. R. Gartia
Department of Mechanical and Industrial Engineering, Louisiana State University, Baton Rouge, LA 70803, USA
mgartia@lsu.edu (M.R.G.)

S. Roy, N. C. Biswa, H. D. Shukla
Department of Radiation Oncology, University of Maryland School of Medicine, Baltimore, MD 21201, USA
Nrusingh.Biswal@umm.edu (N.C.B)
hdshukla@som.umaryland.edu (H.D.S)

D. Burk
Pennington Biomedical Research Center, Baton Rouge, LA 70808, USA

F. Donnarumma
Department of Chemistry, Louisiana State University, Baton Rouge, Louisiana 70803, USA

Y. H. Ko
NewG Lab Pharma, 701 East Pratt Street, Columbus Center, Baltimore, MD 21202, USA

Praveen Kumar Guttula
Sprott Center for Stem Cell Research, Regenerative Medicine Program, Ottawa Hospital Research Institute, Ottawa, ON, Canada

Department of Biochemistry, Microbiology, and Immunology, Faculty of Medicine, University of Ottawa, Ottawa, ON, Canada

H&E imaging analysis

Figure S1A shows morphological changes in the tumor following 3-BP treatment (3-BP) compared to silane treatment (MOCK) using H & E staining. During H&E staining, cell nuclei are stained with hematoxylin (dark blue color), and other structures like cytoplasm are stained with eosin (pink color). Both MOCK and 3-BP tissues consisted of cell nuclei and cytoplasm. Cell nuclei in the silane-treated tissues (MOCK) look more prominent and darker than in the 3-BP groups. Based on the pixel intensity of the images (**Figure S2B**), a significantly higher ($P < 0.001$) cytoplasm content was seen in the 3-BP group compared to the MOCK group. The increase in cytoplasm expression level illustrates that cell division is inhibited in 3-BP-treated tissues compared to the MOCK group.

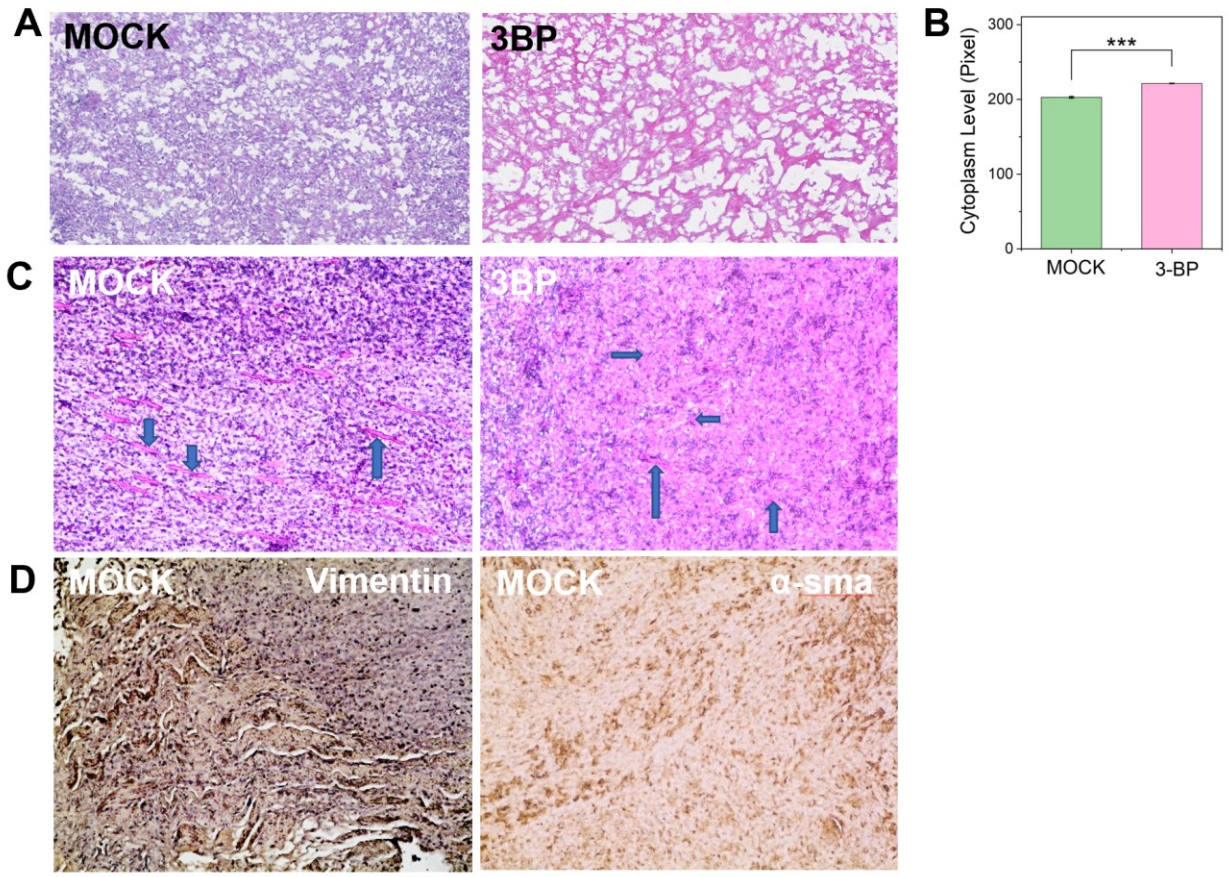

Figure S1. Structural imaging of Pancreatic tumor tissue before and after 3-BP treatment. **(A)** Representative hematoxylin (purple) and eosin (pink) (H&E) stained images of tumor before (MOCK) and after (3-BP) 3-BP treatment. **(B)** Comparison of cytoplasm content of MOCK and 3-BP tissue. The plot shows the pixel intensity differences between the two groups (n =3/group). **(C)** H & E (Hematoxylin and Eosin) stained tissue images. The blood vessels are marked with blue arrows, **(D)** IHC images of MOCK tissue, stained with α-SMA and vimentin, which are cancer associated fibroblast marker.

Raman map analysis using WiRE

As an alternating least square method, the Renishaw Empty Modelling technique works without any previous knowledge and reference spectra. In this method from a collected dataset containing different components, Empty modelling extract distinguishable components spectra (with blue color) with their Raman map images indicating the distribution of the components

withing the Raman image based on the below matrix equation. In the dataset, the Raman spectra of the image (collected spectra of the sample) shows with red color.

$$X = C * S^T + E \quad (1)$$

X is dataset matrix, C image concentration, S extracted spectra, and E error.

Empty Modeling Steps

1- Open collected dataset in WiRE software → Analysis → Mapping Review → In the map selection window choose Empty Modelling → Press create with the following setting.

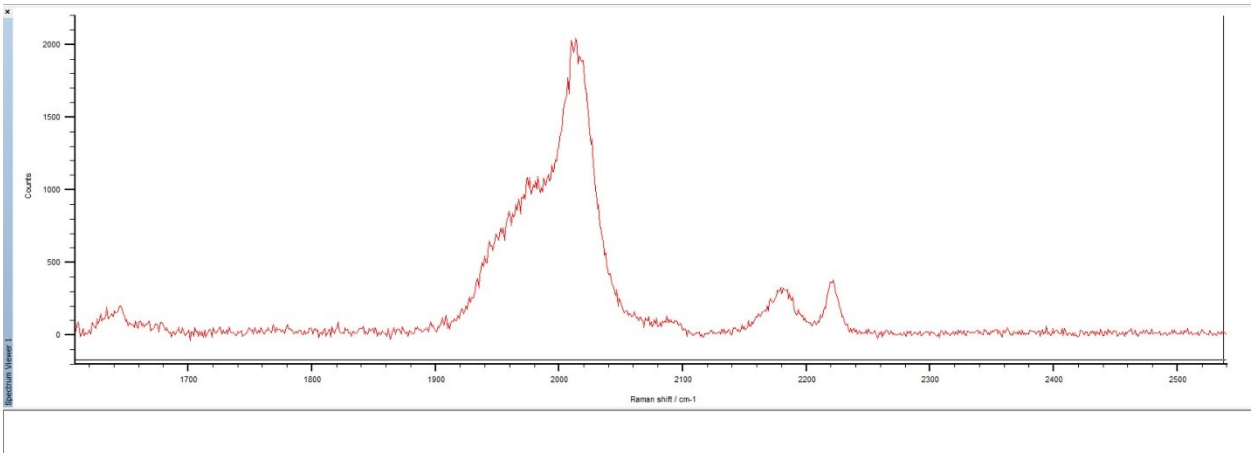

Figure S2. An example of the collected dataset.

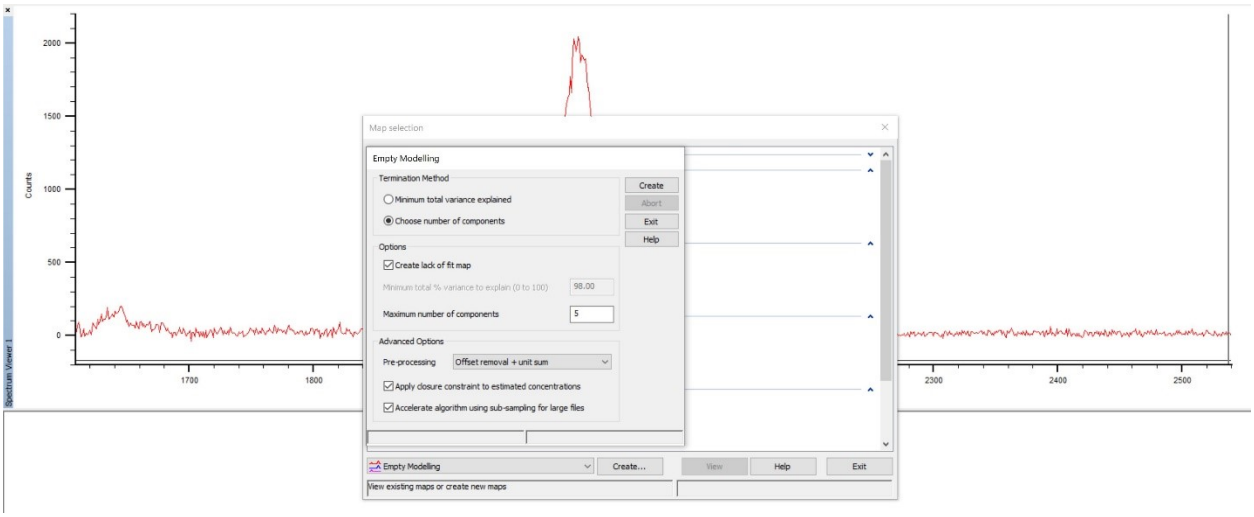

Figure S3. Steps showing how to create Empty Modelling analysis.

Some Examples of Empty Modelling

Figure S4 showing the generated Raman map with its meaningful spectrum. This image was recorded for the MOCK sample probed with SERS nanotags, Au+Dopamine+TPS+TGFβ1. Using the above equation of Empty modelling, it can be seen WiRE generated meaningful spectrum (blue color) with a peak position around 2017 cm^{-1} confirming the presence of SERS nanotag, Au + Dopamine + TPS + TGFβ1. In addition, the concentration of this component is seen with different color distribution throughout the generated mapping image. In this image, dark color shows the area with less probability of the presence of mentioned SERS nanotags, and brighter red color shows the area with high probability of the presence of mentioned SERS nanotags.

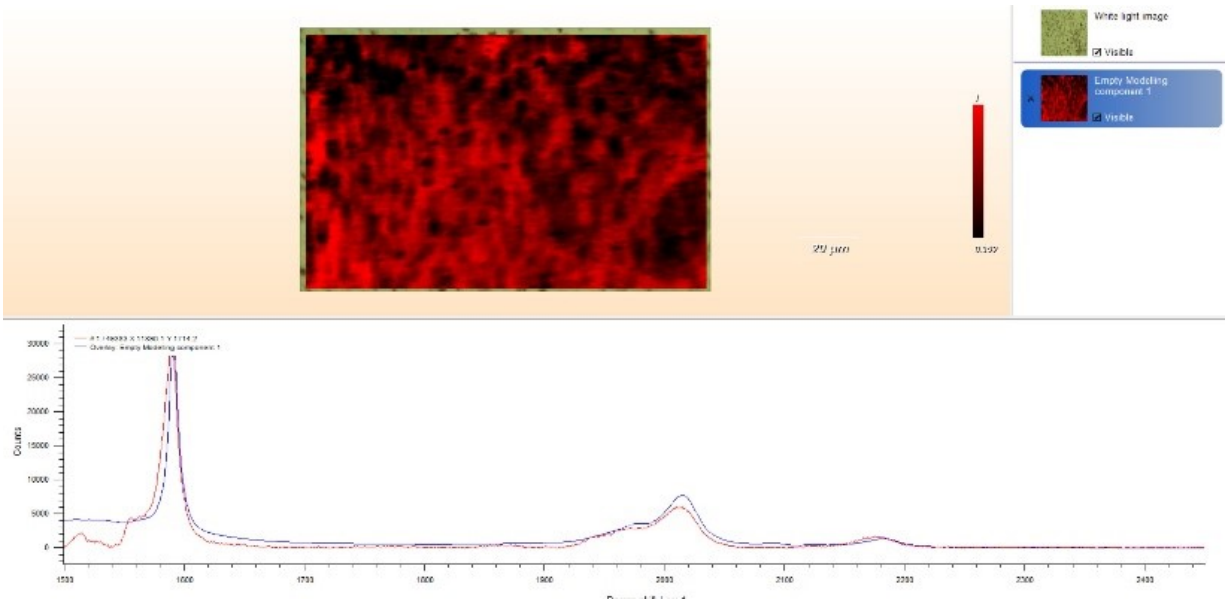

Figure S4. Screenshot of WiRE window after extracting component with its spectrum from the image of MOCK sample probed with Au + Dopamine + TPS + TGFβ1.

Figures S5A-S5D showing the generated Raman maps for three meaningful components with their relative spectra analyzed through Empty Modelling. This image was acquired from the 3-BP sample probed with three different SERS nanotags, (Au + Dopamine + TPS + TGFβ1), (Au + Dopamine + D-6 + Caspase3), (Au + Dopamine + 4-MB + HK2). As can be seen in Fig S5 A, component one with a peak position around 2017 cm^{-1} indicating the presence of Au + Dopamine + TPS + TGFβ1, component two in Figure S5 B with a peak position around 2111 cm^{-1} indicating the presence of Au + Dopamine + D-6 + Caspase3, component three in Figure S5 C, with a peak position around 2228 cm^{-1} indicating the presence of Au + Dopamine + 4-MB + HK2, Figure S5 D without any peak position indicating substrate as its spectrum is not matched with sample spectra (red color). In all images, dark color shows the area with less probability of the presence of mentioned SERS nanotags, and brighter color shows the area with high probability of the presence of mentioned SERS nanotags.

A

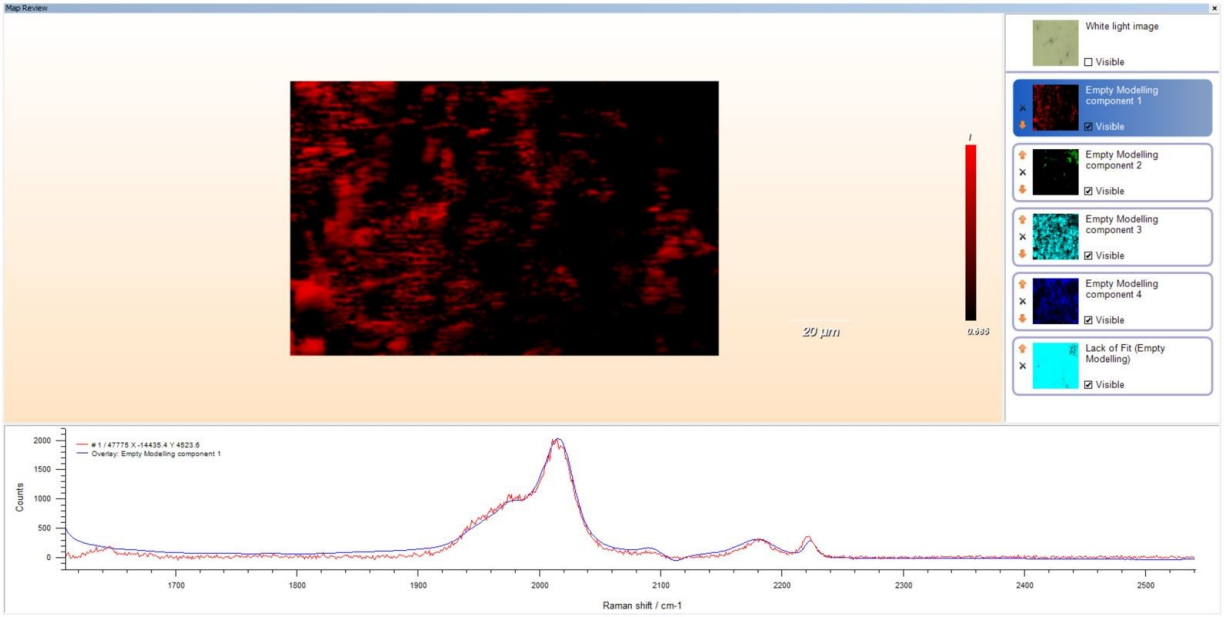
Map Review
White light image
Visible
Empty Modelling component 1
Visible
Empty Modelling component 2
Visible
Empty Modelling component 3
Visible
Empty Modelling component 4
Visible
Lack of Fit (Empty Modelling)
Visible
1
0.995
20 µm
1 / 47775 X -14435.4 Y 4523.6
Overlay: Empty Modelling component 1
Counts
Raman shift / cm-1

B

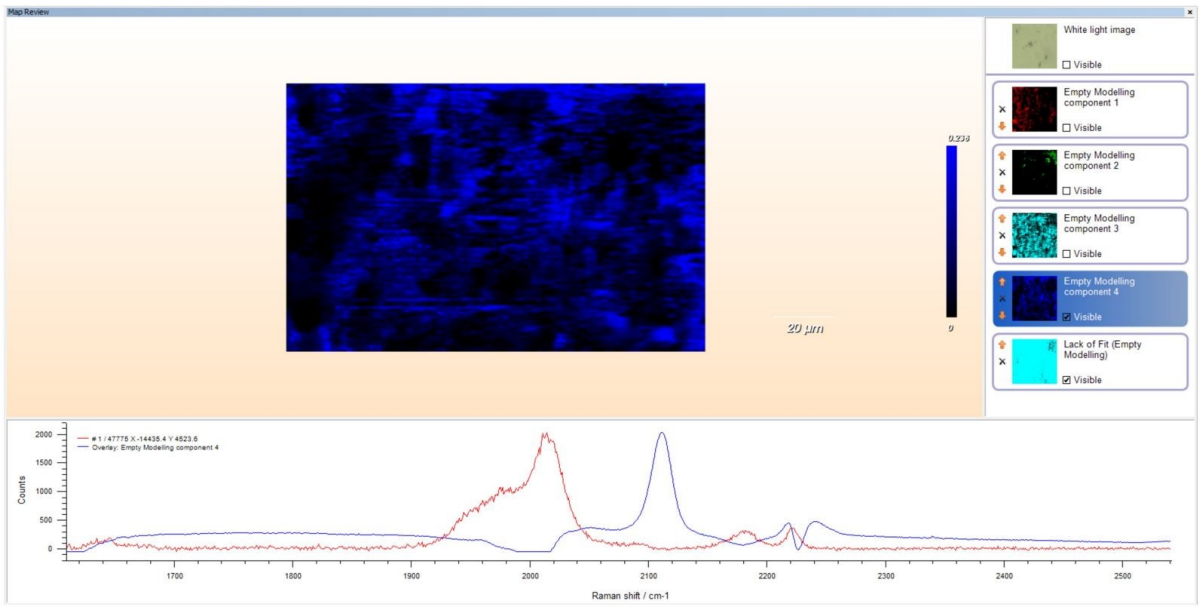
Map Review
White light image
Visible
Empty Modelling component 1
Visible
Empty Modelling component 2
Visible
Empty Modelling component 3
Visible
Empty Modelling component 4
Visible
Lack of Fit (Empty Modelling)
Visible
0.333
0
20 µm
1 / 47775 X -14435.4 Y 4523.6
Overlay: Empty Modelling component 4
Counts
Raman shift / cm-1

C

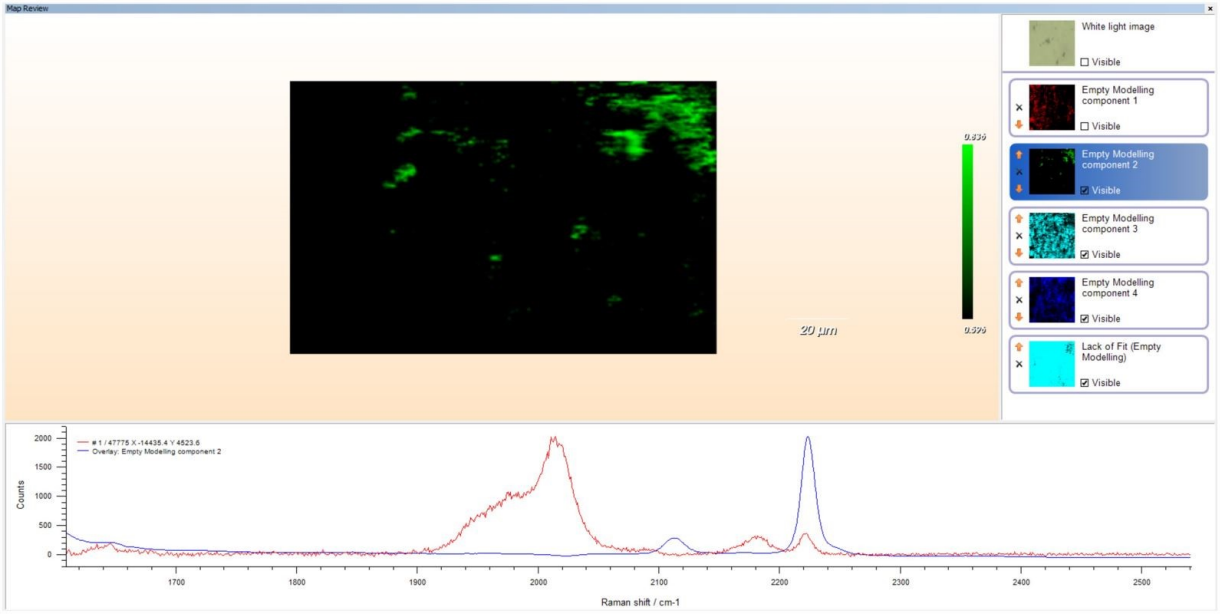

D

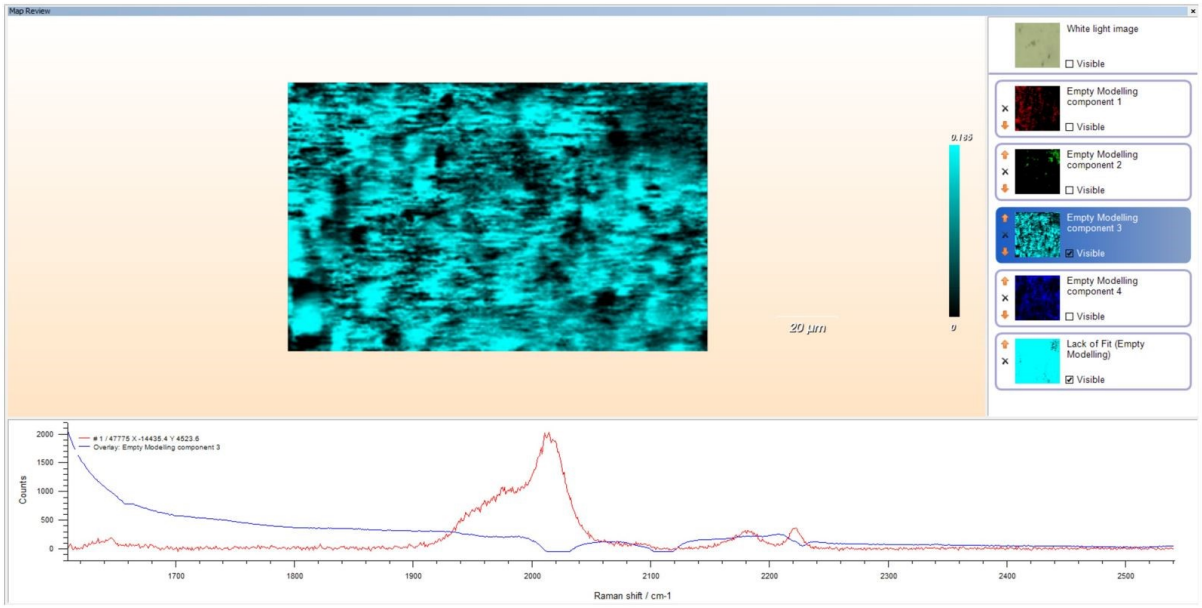

Figure S5. Screenshot of WiRE window after extracting component with its spectrum from the image of 3-BP sample probed with three different SERS nanotags, Au + Dopamine + TPS + TGFβ1, Au + Dopamine + D-6 + Caspase3, Au + Dopamine + 4-MB + HK2. **(A)** generated components with their spectra for Au + Dopamine + TPS + TGFβ1, **(B)** Au + Dopamine + D-6 + Caspase3, **(C)** Au + Dopamine + 4-MB + HK2 (D) substrate.

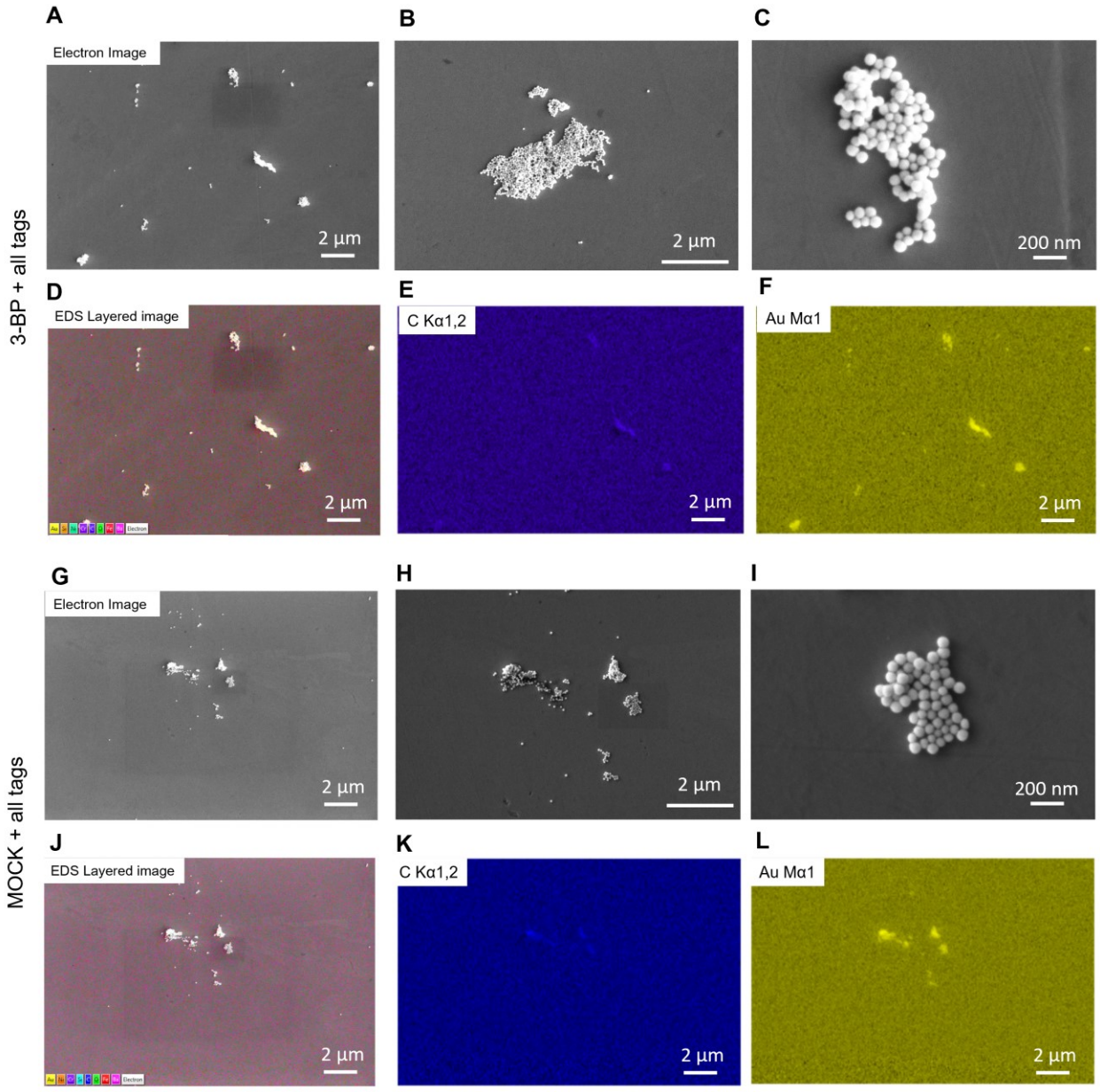

Figure S6. (A) Scanning electron microscopic (SEM) images of the 3-BP tissue probed with all tags (tag1: Au + Dopamine + TPS + TGFβ1; tag2: Au + Dopamine + D-6 + Caspase3; tag3: Au + Dopamine + 4-MB + HK2). **(B,C)** zoomed in image of the AuNPs. **(D)** the corresponding Energy-dispersive X-ray spectroscopy (EDS) image of the tissue **(E)** EDS map of C Kα1,2, and **(F)** EDS map of Au Mα1 surface profile on the tissue. **(G)** Scanning electron microscopic (SEM) images of the MOCK tissue probed with all tags (tag1: Au + Dopamine + TPS + TGFβ1; tag2: Au + Dopamine + D-6 + Caspase3; tag3: Au + Dopamine + 4-MB + HK2). **(H,I)** zoomed in image of the AuNPs, **(J)** the corresponding Energy-dispersive X-ray spectroscopy (EDS) image of the tissue **(K)** EDS map of C Kα1,2, and **(L)** EDS map of Au Mα1 surface profile on the tissue.

ImageJ analysis:

1- Open ImageJ software → Open desired image.

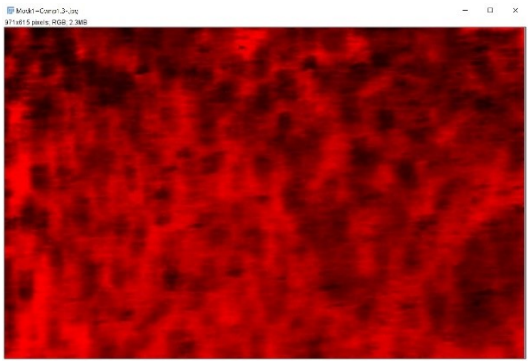

Figure S7. Original image of generated Raman image.

2- Image → Color → Spilt channels to red, green, and blue. For each image, used the associated channel (For image with red color, red channel was selected for intensity measurements)

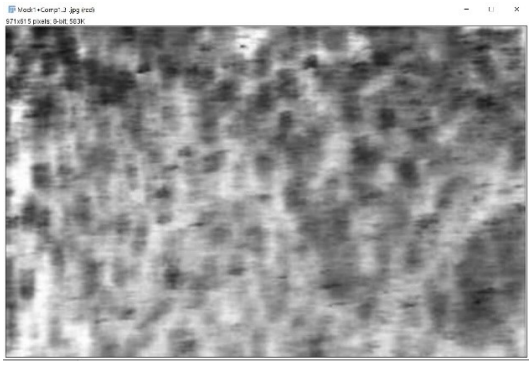

Figure S8. Red channel image after splitting image to three different channels.

3- In the selected channel, using the rectangle icon, 10 different regions were selected to measure the intensity.

4- Analyze → Set measurements (Check Area, Mean Gray Value, Standard Deviation, Minimum, and Maximum) → Analyze → Measure.

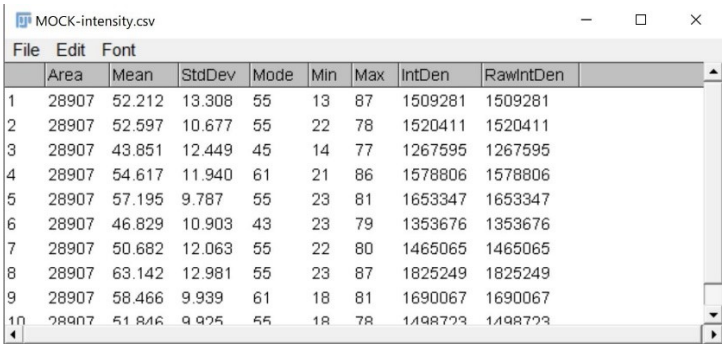

MOCK-intensity.csv

File Edit Font

	Area	Mean	StdDev	Mode	Min	Max	IntDen	RawIntDen
1	28907	52.212	13.308	55	13	87	1509281	1509281
2	28907	52.597	10.677	55	22	78	1520411	1520411
3	28907	43.851	12.449	45	14	77	1267595	1267595
4	28907	54.617	11.940	61	21	86	1578806	1578806
5	28907	57.195	9.787	55	23	81	1653347	1653347
6	28907	46.829	10.903	43	23	79	1353676	1353676
7	28907	50.682	12.063	55	22	80	1465065	1465065
8	28907	63.142	12.981	55	23	87	1825249	1825249
9	28907	58.466	9.939	61	18	81	1690067	1690067
10	28907	51.846	9.925	55	18	78	1498723	1498723

Figure S9. 10 various measurements from the red channel image

5- Used the 10 different mean measurements in MOCK samples and 10 different mean measurements in 3-BP samples to plot bar charts for comparing them using paired comparison feature of Origin software.

Raman Peak Assignment

Table S1. Raman peak positions and their vibrational assignment for TGFβ1

Raman peak position (cm^{-1})	**Assignment**
397	
467	Polysaccharides
504	Cys-Cys S-S stretch
560	Polysaccharides
936	C-C stretch in α helix
1063	C-C, C-N, C-O stretching
1130	C-C asymmetric stretching, C-N stretching,
1250	Amide III in β-sheet

Table S2. Raman peak positions and their vibrational assignment for HK2

Raman peak position (cm^{-1})	**Assignment**
1240	Amide III, antisymmetric phosphate stretching
1454	CH2 or CH3 scissor, /CH2 bending
1680	Amide I in β sheet

Table S3. Raman peak positions and their vibrational assignment for Caspase3

Raman peak position (cm^{-1})	**Assignment**
417	
487	Glycogen
677	Cys C-S stretch
850	Tyrosine
925	C-C stretch in α helix
1058	C-C, C-N, C-O stretching mode
1253	Amide III in β-sheet
1467	CH, CH_2, CH_3 vibrations, NH in plane vibrations
2887	CH2 Stretch
2943	CH_3 Stretch

Table S4. Raman peak positions and their vibrational assignment for Au + Dopamine + TPS

Raman peak position (cm^{-1})	**Assignment**
998	C-C stretch
1174	Cytosine, guanine
1482	
1591	C=C stretch
2018	$-C \equiv C-$
2183	

Table S5. Raman peak positions and their vibrational assignment for Au + Dopamine + D-6

Raman peak position (cm^{-1})	**Assignment**
2116	C-H/C-D symmetric stretching
2242	C-H/C-D antisymmetric stretching

Table S6. Raman peak positions and their vibrational assignment for Au + Dopamine + 4-MB

Raman peak position (cm^{-1})	**Assignment**
363	wagging of Au-CN
583	
1074	C-C bond of the benzene ring
1177	symmetric C-N stretching
1585	symmetric benzene ring stretching ring
2225	C≡N

Table S7. Comparison of Raman peak positions for all the Raman reporters

Tag1 (TGFβ1 +TPS)	**Tag2 (Caspase3 +D-6)**	**Tag3 (HK2 +4-MB)**	**All tags (tag1+tag 2 +tag3)**	**TGF β1**	**Caspase 3**	**HK2**	**TPS**	**D-6**	**4-MB**	**Raman band range (cm^{-1})**
		584		397						300-400

					417					400-450
				467	487					450-500
506 527				504						500-550
			583	560						550-600
			646				646	622		600-650
	650				677					650-700
										700-750
								765	777	750-800
					850					800-900
999	993		999	936	925			999		900-1000
1025	1031	1076	1076	1063	1058		1001		1073	1000-1100
1130 1175		1177	1176	1130					1184	1100-1200
1200 1245		1200	1200	1250	1253	1240	1221		1204	1200-1300

1380										1300 - 1400
1482	1438	1476	1482		1467	1454	1489	1484		1400 - 1500
1592		1586	1592				1600		1592	1500 - 1600
	1651	1648				1680				1600 - 1700
2017			2018					2006		2000 - 2100
2183	2111		2112				2160	2132		2100 - 2200
	2231	2228	2224					2259	2227	2200 - 2300
	2847				2887					2800 - 2900
					2943					2900 - 3000

Table S8. Result of Pearson correlation coefficient calculated from Raman and LC-MS results.

Lipids								
		Raman				**LC-MS**		**Pearson R**
	MOCK	3-BP	3-BP/MOCK		MOCK	3-BP	3-BP/MOCK	
TG	0.3389	0.3875	1.1434		463895.7	473073	1.0198	
CL	-0.2337	0.17751	-0.7596		263064.6	232953.9	0.8855	0.9935
PC	0.21331	-0.15976	-0.7490		243074.8	210828.8	0.8673	

Table S9. Result of Pearson correlation coefficient calculated from Raman and IHC results.

			Proteins					
		Raman				**IHC**		
	MOCK	3-BP	3-BP/MOCK		MOCK	3-BP	3-BP/MOCK	**Pearson R**
TGFB1	53.1437	13.3993	0.2521		47.538	1.757	0.0370	
HK2	48.144	14.5238	0.3017		32.442	2.024	0.0624	0.9999
Caspase3	7.9435	23.881	3.0064		6.745	91.28	13.5330	

Table S10. Redox ratio measured by SHG and FLIM.

		Redox ratio	
	MOCK	3-BP	3-BP/MOCK
SHG	0.6704	0.8806	1.3135
FLIM mean lifetime	0.1885	0.3365	1.7851
FLIM (A_2/A_1)	0.057764	0.216282	3.7442

Table S11. Collagen expression level measured by SHG, PSR, and Polarization methods.

		Collagen	
	MOCK	3-BP	3-BP/MOCK
SHG	23.67687	8.98353	0.3794
PSR	143.4695	130.1647	0.9073
Polarization	15.06993	7.98683	0.5299